

Large-scale natural fracture network patterns: Insights from automated mapping in the Lilstock (Bristol Channel) limestone outcrops

Rahul Prabhakaran^{a,b,1}, J L Urai^{d,2}, G Bertotti^{a,3}, C Weismüller^{c,4}, D M J Smeulders^{b,5},

^a*Department of Geoscience and Engineering, Delft University of Technology, Delft, the Netherlands*

^b*Department of Mechanical Engineering, Eindhoven University of Technology, Eindhoven, the Netherlands*

^c*Neotectonics and Natural Hazards, RWTH Aachen University, Aachen, Germany*

^d*Structural Geology, Tectonics and Geomechanics, RWTH Aachen University, Aachen, Germany*

^{a,b,1} *corresponding author: R.Prabhakaran@tudelft.nl*

^{d,2} *J.Urai@ged.rwth-aachen.de*

^{a,3} *G.Bertotti@tudelft.nl*

^{c,4} *C.Weismueller@nug.rwth-aachen.de*

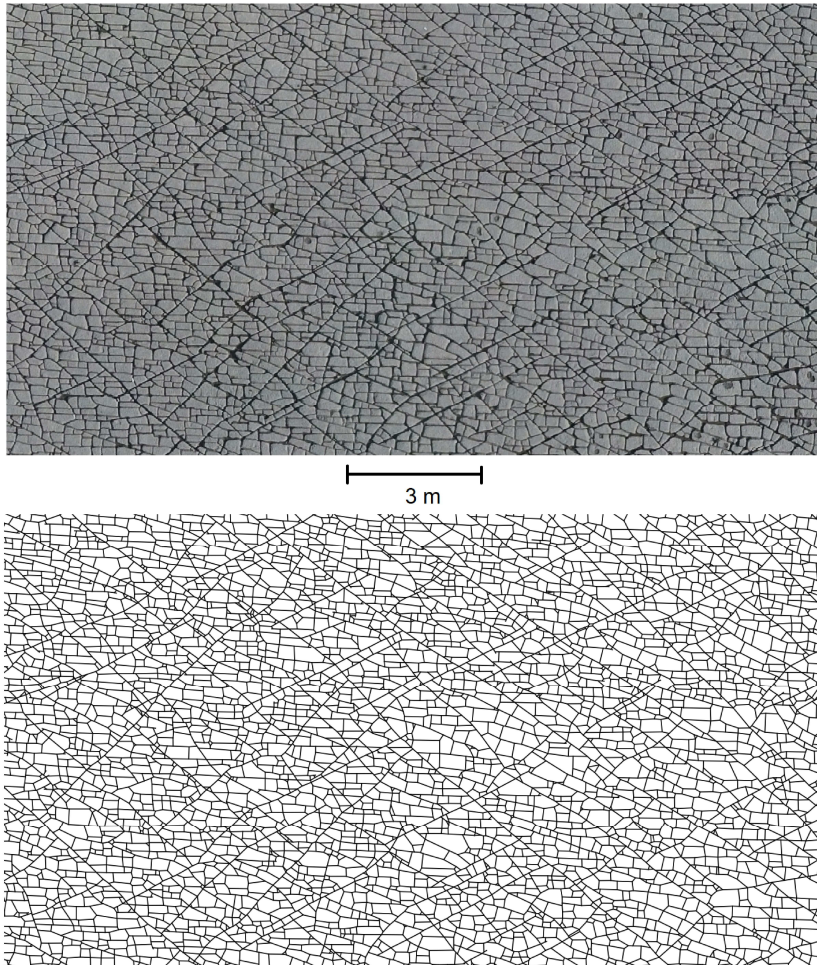
^{b,5} *D.M.J.Smeulders@tue.nl*

This manuscript is a non-peer reviewed preprint that has been submitted to the Journal of Structural Geology.

Graphical Abstract

Large-scale natural fracture network patterns: Insights from automated mapping in the Lilstock (Bristol Channel) limestone outcrops

Rahul Prabhakaran, J L Urai, G Bertotti, C Weismüller, D M J Smeulders,



Highlights

Large-scale natural fracture network patterns: Insights from automated mapping in the Lilstock (Bristol Channel) limestone outcrops

Rahul Prabhakaran, J L Urai, G Bertotti, C Weismüller, D M J Smeulders,

- A complete, large-scale, vectorized dataset of natural fracture networks from nearly 17,000 sq. m of horizontal limestone layers was prepared by fully automated interpretation of the famous benches at Lilstock, Bristol Channel, UK
- Dataset comprises nearly 350,000 fractures extracted from UAV photogrammetric images using automatic tracing with complex shearlet transform and manually validated for topological and spatial accuracy
- Geologically relevant fractures are automatically extracted from spatial graph segments using a set of functions that simplifies the manual interpretative task of identifying fracture segments from tip-to-tip
- P_{20} , P_{21} , node degree distributions, length distributions, and area distributions
- The dataset is valuable as input for further investigations into interpretation of fracture generations, intra-network spatial variability of fracture networks and as static models for fluid-flow and geomechanical simulation

Large-scale natural fracture network patterns: Insights from automated mapping in the Lilstock (Bristol Channel) limestone outcrops

Rahul Prabhakaran^{a,b,1}, J L Urai^d, G Bertotti^a, C Weismüller^c, D M J Smeulders^b,

^a*Department of Geoscience and Engineering, Delft University of Technology, Delft, the Netherlands*

^b*Department of Mechanical Engineering, Eindhoven University of Technology, Eindhoven, the Netherlands*

^c*Neotectonics and Natural Hazards, RWTH Aachen University, Aachen, Germany*

^d*Structural Geology, Tectonics and Geomechanics, RWTH Aachen University, Aachen, Germany*

Abstract

The Lilstock outcrop in the southern Bristol Channel provides exceptional outcrop of several limestone layers with stratabound fracture networks, providing the opportunity to create a very large, complete, and ground-truthed fracture model. Here we present the result of automated fracture extraction of high-resolution photogrammetric images (0.9 cm/pixel) of the full outcrop, obtained using an unmanned aerial vehicle, to obtain a very large, full-resolution, map of the complete fracture network with nearly 350,000 ground-truthed fractures. We developed graph-based functions to resolve some common issues that arise in automatic fracture tracing such as incomplete traces, incorrect topology, artificial fragmentation, and linking of fracture segments to generate geologically significant trace interpretations. The

Email address: R.Prabhakaran@tudelft.com (Rahul Prabhakaran)

fracture networks corresponding to different regions within the outcrop are compared using several network metrics and the results indicate both inter- and intra-network (layer to layer) structural variabilities. The dataset is a valuable benchmark in the study of large-scale natural fracture networks and its extension to stochastic network generation in geomodelling. The dataset also highlights the intrinsic spatial variation in natural fracture networks that can occur even in weakly-deformed rocks.

Keywords: , fractured pavements, natural fracture networks, carbonates, spatial graphs, graph theory, discrete fracture networks

1. Introduction

1 Fractures in rocks can form networks with fracture tips forming abutting or
2 cross-cutting physical interactions with other fractures or remaining isolated
3 within rock matrix. The evolution into a final, cumulative network depends
4 on the interplay of multiple processes which can be highly non-linear with
5 different levels of spatio-temporal feedbacks. The spatial arrangements of
6 fracture networks can be a significant geomorphic agent, influencing land-
7 scape evolution processes (Scott & Wohl, 2019), serve as dissolution path-
8 ways for karstic cave formation (Boersma et al., 2019; Bertotti et al., 2020),
9 and influence subsurface fluid flow patterns that are relevant for hydrogeolog-
10 ical, geo-energy and waste disposal applications (National Research Council,
11 1996; Berkowitz, 2002). Given such non-trivial influences, it is important to
12 be able to characterize and compile, from a network perspective, a typology
13 of fracture patterns.

14 Mechanistic numerical modelling of fracture propagation and subsequent

fracture network formation can include complex physics pertaining to individual fractures such as fracture tip behaviour, fluid driven fracturing, interaction of propagating fractures with pre-existing discontinuities and other propagating fractures (Laubach et al., 2019). Such mechanistic models can be based on finite elements (for e.g., Thomas et al., 2018, 2020 etc), extended finite element methods (such as Remij et al., 2015; Valliappan et al., 2019 etc), discrete element methods (such as Virgo et al., 2016; Guo et al., 2017 etc), boundary element methods (such as Olson, 2004; Olson et al., 2009 etc), and phase-field methods (such as Yoshioka & Bourdin, 2016; Lepillier et al., 2020 etc), and differ in the way rock substrate and propagating fracture are numerically treated. Such complex models are computationally intensive and do not scale to the problem of large-scale network evolution. Recent developments include quasi-mechanical approaches in which fracture networks genetically evolve from flaws without resorting to rigorous geomechanical treatment (Lavoine et al., 2020; Welch et al., 2019) but large-scale network development is still difficult to realize.

In such a context, outcrop-derived networks holds relevance. The advantage of outcrops is that they implicitly encode spatial organization of networks and their properties can be observed and sampled when outcrop quality permits. The proliferation of UAV photogrammetry has lead to an increase in both volumes and speed of acquisition of digital outcrop data (Bemis et al., 2014; Hodgetts, 2013). Coupled with automatic image processing tools, it is now possible to obtain outcrop-derived 2D discrete fracture networks (DFNs) at large enough scales that can enhance our understanding of geometrical organization and spatial heterogeneity of natural fracture net-

40 works (Palamakumbura et al., 2020).

41 Outcrop-based characterization of natural fractures typically involves frac-
42 ture sampling methods such as the use of scanlines (1D), fracture traces
43 from orthorectified fractured rock images (2D), fracture traces from LIDAR
44 (pseudo-2D), and geophysical imaging such as ground penetrating radar and
45 tomography (3D). Recent advances in fracture characterization utilize data-
46 fusion techniques in which multi-spectral, hyperspectral, gravity, and mag-
47 netic remote sensing are combined in outcrop studies. Additionally, geo-
48 chemical methods such as dating of geofluids from veins and spectroscopy
49 on vein infill minerals provide information in relative timing or episodes of
50 fracturing (Becker et al., 2010; Laubach et al., 2016). The combination of
51 these techniques incorporates high-degrees of geological realism in contrast
52 to stochastically-generated DFNs based on sparse data, commonly used in
53 fractured reservoir modelling, that do not fully replicate natural fracture pat-
54 terns (Bisdom et al., 2014; Thovert et al., 2017). In this contribution, we
55 restrict the scope of fracture characterization to the mapping of 2D frac-
56 ture traces from photogrammetric remote sensing methods at the Lilstock
57 outcrop, Bristol Channel, UK which exposes multiple fractured limestone
58 layers. (Peacock, 2004; Rawnsley et al., 1998; Engelder & Peacock, 2001;
59 Belayneh et al., 2006; Weismüller et al., 2020).

60 We build on the first (Weismüller et al., 2020) and second (Passchier
61 et al., 2021) part of this project. The complex shearlet transform method
62 (Reisenhofer et al., 2016; Prabhakaran et al., 2019) is used to automatically
63 extract fracture traces from high resolution photogrammetric data published
64 by Weismüller et al. (2020). A critical comparison between automatic and

65 manual tracing was presented in Weismüller et al. (2020) using topological
 66 relationships, fracture intensity, and fracture density measures, and showed
 67 that the quality of automatic tracing is consistent with the interpretations of
 68 a proficient interpreter. Weismüller et al. (2020) covered five regions of 140
 69 sq. m each within the Lilstock pavement while Passchier et al. (2021) has
 70 mapped the different fracture generations but incompletely. In this work,
 71 the automatic tracing is extended to an area that is 20 times larger resulting
 72 in a rich dataset that amounts to nearly 350,000 fractures.

73 **2. Fractures as Spatial Graphs**

74 Multiple authors have suggested the use of graph theory and spatial graph
 75 representations to represent fracture networks (Manzocchi, 2002; Valentini
 76 et al., 2007a,b; Sanderson et al., 2019; Santiago et al., 2016). Such a repre-
 77 sentation maintains topological relationships between fracture segments and
 78 spatial relationships between fracture edges. Topology plays a major role
 79 in connectivity of the fracture network which has important implications for
 80 fractured hydrogeologic and subsurface modelling (Berkowitz, 2002). Frac-
 81 ture networks share similarities with other spatial networks such as road
 82 networks, power grid infrastructure, and plant leaf skeletons in that steric
 83 constraints impose limitations on the maximum degree of a node. This is
 84 not a constraint for non-spatial graphs such as social networks, citation net-
 85 works etc where node degrees can be very large without encountering phys-
 86 ical constraints on edge addition (Barthelemy, 2018). Therefore, methods
 87 and techniques developed for spatial graphs can be easily extended to frac-
 88 ture network data. A graph representation is advantageous as every graph

89 is associated with a variety of matrices such as adjacency, laplacian, inci-
 90 dence, etc. This allows the use of linear algebra techniques and algorithms
 91 to investigate properties of the graph structure and derive insights into the
 92 spatial and spectral properties. Within the structural geology literature, such
 93 approaches are not widespread as data pipelines that can deliver sufficient
 94 volumes of fracture data in the form of graphs face several challenges in data
 95 acquisition and processing. The advent of UAV-based data acquisition and
 96 automatic fracture trace extraction opens up new avenues to use prevailing
 97 graph algorithms to extract insights from large-scale fracture patterns.

98 From graph theory, a *graph* is a pair $G = (V, E)$ with V being a set of
 99 *vertices* and E , a set of *edges*. The abstraction that connects mathematical
 100 graph theory to fracture networks is that fracture intersections form the
 101 vertex set, V and fracture segments linking the vertex set V form the edge
 102 set, E . When a spatial positioning data structure is additionally specified
 103 to represent position of each fracture intersection in 2D cartesian space, the
 104 fracture network forms the planar graph, G_p . An example of a fracture
 105 network represented as a graph is depicted in Fig.1(a) The corresponding
 106 graph with spatial positioning is depicted in Fig.1(b).

107 In this representation, the definition of a geological fracture ' F ', is simply
 108 a subset of ' m ' connected edges within the graph $F_E \subset G$. This is also
 109 equivalent to a subset of ' $m + 1$ ' nodes which are contained within the edge
 110 set that forms a walk or path within the graph (see Fig.2). The entire fracture
 111 network is a list of paths which are specific sequences of nodes (and edges).
 112 A *weighted* graph is one in which the edge set is associated with weights
 113 that can represent, for instance, the relative importance of edges within the

114 complete edge list. In case of fracture networks, this may simply be the
115 euclidean distance between the end nodes of the particular edge. A graph
116 may be *directed* and referred to as a *digraph* which implies that an edge has
117 a source node and a target node. In case of fracture networks, an *undirected*
118 graph representation is sufficient.

119 The graph representation where fracture intersections form vertices and
120 fracture segments form edges, is called the *primal* form (Barthelemy, 2018).
121 There is also a *dual* form of a graph in which fractures from tip-to-tip form
122 graph nodes and interconnections between fractures form the edges. Such
123 *dual* representations have been used by Valentini et al. (2007b), Andresen
124 et al. (2013), and Vevatne et al. (2014) for fracture networks. To illustrate
125 the difference, an example network from Bisdom et al. (2017) is depicted
126 in the primal form in Fig.3.(a) and in the dual form in Fig.3.(b). It can be
127 observed that the longest fracture striking NW-SE has the maximum number
128 of intersections with smaller fractures abutting on to or cross-cutting it. The
129 longest fracture is therefore the node with the highest degree in the dual
130 graph. Since the dual representation considers only topological connections
131 between fractures from tip-to-tip, we do not associate any spatial position to
132 the nodes in Fig.3.(b). Figure.3.(c) and Fig.3.(d) depict adjacency matrices
133 of the primal and dual graphs respectively. The degree distributions of the
134 primal and dual are depicted in Fig.3.(e) and Fig.3.(f) respectively. The node
135 degrees in the primal are subject to geometric constraints with a maximum
136 degree of 6 (a hexa type joint). The dual graph degree distribution is more
137 spread out with 64 being the largest degree.

138 By converting fracture network shapefiles to primal graphs, we can then

139 use graph algorithms and metrics to analyze the networks. Various network
140 metrics can be used to quantify inter- and intra-network variability in fracture
141 networks using the graph representation. This is a novel approach in fracture
142 network analysis in the Geosciences, made possible by the large amount of
143 fractures. We propose that our results form a valuable benchmark for future
144 fracture mapping and characterisation methods, and provide all images and
145 mapped fractures for further study. The network data and the code used is
146 available as supplements with this contribution for the benefit of researchers
147 interested in natural fracture characterisation.

148 **3. Geology of the Study Area**

149 The outcrops studied in this paper are located off the southern coast of the
150 Bristol Channel in West Somerset, UK, close to the hamlet of Lilstock (see
151 Fig.4). The area is within a 7.428 sq.km geological Site of Special Scientific
152 Interest (SSSI), referred to as the Blue Anchor to Lilstock Coast SSSI, due
153 to the exposures ranging from Early Jurassic to Lower Lias. Deformation
154 features such as faults, fractures, and joints are exposed within the study
155 area (Spruženiece et al., 2020). The layers of interest are three fractured
156 limestone pavements referred to as *benches* by Loosveld & Franssen (1992).

157 We focus on five fractured pavements the extent of which is depicted in
158 Fig.5. The chosen regions correspond to the northern limb of a single E-W
159 trending anticline formed during the N-S compression phase (Dart et al.,
160 1995). The fractured regions of interest are designated as Areas 1-5. Areas 1
161 & 3 and Areas 2 & 4 belong to the same stratigraphic layer. The particular
162 areas were chosen as they are largely devoid of vegetation and weathering

163 and contain joints belonging to different stages in the tectonic history forming
 164 a well-connected spatial network. Additionally, the studied regions contain
 165 sub-regions which were the focus of previous work by Loosveld & Franssen
 166 (1992), Rawnsley et al. (1998), Engelder & Peacock (2001), Belayneh & Cos-
 167 grove (2004), Belayneh (2004), and Gillespie et al. (2011). The relationship
 168 between joints described in the above-mentioned works is discussed by Pass-
 169 chier et al. (2021).

170 *3.1. Structural History*

171 The structural history of the region may be classified into several tec-
 172 tonic phases. Beginning with N-S extension in the Early Jurassic to Early
 173 Cretaceous and again in the Late Cretaceous to Oligocene (Rawnsley et al.,
 174 1998), these events are evidenced by E-W striking normal faults (Brooks
 175 et al., 1988). These extension events were followed by N-S Alpine compres-
 176 sion during the late Oligocene to Miocene resulting in inversion of normal
 177 faults and gentle folding, followed by progressive relaxation during the Late
 178 or post-Miocene (Rawnsley et al., 1998). Normal faults and conjugate strike
 179 slip faults indicate this event (Dart et al., 1995; Glen et al., 2005; Kelly
 180 et al., 1999; Nemčok et al., 1995). This was followed by burial of up to 1.5
 181 km and exhumation with features such as small folds, faults, veins, and joints
 182 (Rawnsley et al., 1998; Hancock & Engelder, 1989).

183 *3.2. Previous descriptions of jointing*

184 The Mode-I joints exposed in the Lilstock are bedding-perpendicular and
 185 largely stratabound with apertures enhanced by tide-induced dissolution,
 186 ranging from sub-millimeter at the bottom to an order of centimetres at

187 the bed top (Gillespie et al., 2011). The decimeter thick limestone layers
188 are intercalated with claystone layers of the order of $10^0 - 10^2$ cm thick-
189 nesses. A striking feature of the jointing is the network that is formed due to
190 joints abutting or cross-cutting each other. The presence of small displace-
191 ment faults within the bench cause visibly identifiable variations in fracture
192 patterns and intensities. The Lilstock outcrop also contains several long,
193 fan-shaped joints that emanate from asperities on faults (Rawnsley et al.,
194 1998). These joint fans have also been described in other outcrops near the
195 Bristol Channel in similar lithologies (Bourne & Willemse, 2001).

196 The joints are believed to be due to minor tectonic events that post-dated
197 the stress inversion. Various authors have interpreted jointing histories and
198 number of joint sets based on observations within sub-regions of the outcrop.
199 Loosveld & Franssen (1992) identified six joint sets based on orientation.
200 Rawnsley et al. (1998) identified four main joint sets using characteristics
201 such as orientation, length, and spacing. Engelder & Peacock (2001) iden-
202 tified six jointing sets based on orientation and abutting criteria. Belayneh
203 (2004) identified six joint sets based on orientation, length, and aperture.
204 More recent work by Wyller (2019) distinguished ten jointing generations us-
205 ing abutting relationships, length, and orientation. These above-mentioned
206 attempts at delineating jointing generations are limited to certain regions
207 within the entire outcrop (see Fig.5). Passchier et al. (2021) utilized the
208 same image dataset as ours and was able to identify eight generations of
209 joints from manually traced fractures that include all regions covered by the
210 previous studies. The criteria used by Passchier et al. (2021) to partition indi-
211 vidual fractures into jointing generations consisted of combination of length,

orientation, and abutting criteria. The results highlighted considerable spatial variability in jointing with some regions containing just 2-3 generations while other areas achieved saturation with the maximum eight sets.

Rawnsley et al. (1998) associate the earliest joint sets as forming sub-parallel to regional Alpine compression, with subsequent jointing sets being perturbed by faults and influenced by anticlockwise shift of maximum horizontal stress during basin-wide relaxation of Alpine compression. The youngest joints were proposed to be correlated with relaxation or contracting of rock. Engelder & Peacock (2001) suggested that joint formation is linked to minor tectonic events postdating the basin inversion. The youngest joints are proposed to be coorelated with the contemporary stress field (Engelder & Peacock, 2001) or due to exhumation in a late stage of the Alpine stress field (Hancock & Engelder, 1989). Dart et al. (1995) proposed that the jointing patterns involve overprinting of joint generations.

4. Methods

4.1. Photogrammetric Dataset

The image data that we consider in this work is extracted from UAV-derived orthoimagery published as a dataset (Weismüller et al., 2020). The full dataset comprises of orthomosaics generated from UAV flights at 10 m, 20 m, 25 m, and 100 m. We utilize the orthomosaics acquired between 20-25 m flight altitude resulting in imagery of 0.9 cm/pixel. Weismüller et al. (2020) used this value of resolution to manually interpret fractures in five 140 sq.m regions within Areas 2 and 4 (see Fig.5) and quantitatively compared these automatic interpretations. The validation of manual with respect to

automatic mapping indicated closely similar fracture patterns, generating confidence in an endeavour to extend the automatic interpretation to larger regions of the outcrop over multiple layers. Passchier et al. (2021) used the same image dataset with similar resolution to identify jointing generations from manual interpretations within Areas 2 and 4.

4.2. Automatic tracing workflow

The complex-shearlet transform (Reisenhofer et al., 2016) was extended to automatic outcrop-scale fracture trace extraction from UAV photogrammetry by Prabhakaran et al. (2019). The workflow comprises of a series image processing steps which is depicted in Fig.6. The steps include complex shearlet-based ridge detection, thresholding, skeletonization and polyline fitting. The image data is divided into sub-tiles of 1000 x 1000 pixels for efficient computation and considering memory requirements. The processing steps are then applied to each tile separately. This splitting of the images therefore enables processing on multiple workstations. The realized vector geometries are combined into shapefiles. The number of image tiles that correspond to each bench is summarized in Table.1 along with approximate areal extent.

Since quality of automatic fracture detection depends on enlarged discontinuities owing to weathering or otherwise and given that the degree of weathering is spatially variable, a single set of parameters is insufficient to efficiently extract all exposed traces. Therefore, three different sets of shearlet parameters are used for ridge detection yielding three different ridge image ensembles (E_1, E_2, E_3) that capture fractures both subtle and well-eroded. The three shearlet system parameters used are listed in the data supplement.

261 Various linear combinations (a, b, c) are applied to E_1, E_2, E_3 to obtain an
262 optimal E_{final} for each image tile as per

$$263 \quad E_{final} = aE_1 + bE_2 + cE_3.$$

264 This combined ensemble, E_{final} , is then used for further image processing
265 as per the workflow in Fig.6. The traces extracted from each image tile
266 is then merged as a single shapefile. An example of an image tile with
267 a ridge ensemble and the corresponding vectorized shapefile is depicted in
268 Fig.7. Though the Lilstock outcrop is a high-quality exposure, there are still
269 sources of false positives owing to erosion, water puddles, shrubbery, and
270 rubble. These artefacts are removed manually using interactive GIS tools.
271 The total time taken for automatic mapping for all tiles was 384 hours CPU
272 time. The time taken to clear the artefacts varies between 1-2 hours per
273 image tile depending upon the image.

274 *4.3. Shapefiles to Graphs*

275 The automatic traces are in the form of shapefiles. We developed MAT-
276 LAB routines to enable conversion of shapefiles of fracture networks into
277 graph data structures and vice-versa. The conversion results in a primal
278 graph, which can then be converted to a dual graph if the sequence of primal
279 graph edges that correspond to a complete fracture from tip-to-tip can be
280 specified. The graph representations can then be exported in various graph
281 formats that are readable by graph visualization software and packages such
282 as Gephi (Bastian et al., 2009), iGraph (Csardi & Nepusz, 2006), and Net-
283 workX (Hagberg et al., 2008).

284 4.4. *Making graph representations geologically meaningful*

285 The use of automatic tracing may produce fractures that deviate from
286 a manual interpretation. When interpreting by hand, an interpreter utilizes
287 multiple cues to trace a fracture from tip-to-tip and identify fracture tip
288 topologies. Therefore, using ubiquitous network metrics such as cumulative
289 length distributions, rose plots, topological summaries on automatically ex-
290 tracted traces can result in skewed results. To this end, we developed a series
291 of graph manipulation routines that take the raw graph data input generated
292 from the automatic traces into geologically meaningful data. This workflow
293 is summarized in Fig.8 and further described in the following sections. The
294 code supplement contains the implementations of the functions.

295 4.4.1. *Topological discontinuities*

296 Automatically traced interpretations can contain topological discontinu-
297 ities. By analysing automatically-traced networks and comparing them with
298 manual interpretations, we classify connectivity issues and design specific
299 routines to resolve these discontinuities. The three most common topologi-
300 cal errors are depicted in Fig.9. These include situations when

- 301 • a degree-1 node is in close proximity to a degree-2 node with near
302 orthogonal angles
- 303 • a degree-3 (or Y-node) is present as three closely spaced degree-1 nodes
- 304 • two degree-2 nodes with sharp orthogonal angles are in close proximity

305 In order to resolve these topological errors in connectivity, we perform a
306 delaunay triangulation (De Berg et al., 2000) on the fracture spatial graphs

307 using the nodes as control points. The triangulation creates tri-elements
308 around the fracture traces. By inspecting the histograms of tri-element ar-
309 eas, anomalous elements with very small areas can be isolated. These small
310 tri-elements are formed at the regions of topological errors or with very high
311 aspect ratios. Using a suitable cut-off area that is determined by visual in-
312 spection of the small tri-element areas, graph manipulations are performed
313 on the graphs that resolve the loss of connectivity depending upon the node
314 types and edge properties involved. The manipulations involve adding / re-
315 moving edges and nodes and updating the fracture graph. The three types
316 of manipulations that are done to rectify topological discontinuities are il-
317 lustrated in Fig.10. The code implementations are attached within the code
318 supplement.

319 *4.4.2. Resolving artificial fragmentation of fracture segments*

320 Artificial fragmentation of fracture trace happens when traces appear to
321 be connected and topologically correct to visual inspection but split and saved
322 separately within the shapefile attribute tables. This kind of situation can
323 happen due to tile-wise image processing where fracture polylines that are
324 otherwise continuous, are fragmented and saved as a cascade of isolated seg-
325 ments. Other reasons are due to the way polylines are fitted to skeletonized,
326 binary pixel clusters as per the workflow in Fig.6. The skeletonization proce-
327 dure specifies branch points between intersecting fractures. However, due to
328 varying ridge thickness within the image, it is sometimes possible that seg-
329 ments are connected but are incorrect labelled from a geological perspective.
330 Such a situation is depicted in Fig.11(a).

331 In order to be geologically consistent, the visually continuous but discon-

332 nected segments have to be combined into a single polyline entity. We develop
 333 a graph edge linking function that first identifies all degree-2 nodes within
 334 the graph. For these nodes, node neighbours with degree 2 are identified and
 335 appended into a preliminary node path. The end nodes of the node path
 336 are queried again for further neighbour nodes having degree-2 and repeated
 337 till there are no more such nodes in either direction of the node path. The
 338 resulting node path is now a single connected polyline representing a fracture
 339 segment. The implementation is attached within the code supplement. The
 340 effect of the edge linking is depicted in Fig.11(b).

341 4.4.3. *Resolving step-outs*

342 Automatically identifying fracture edges that belong to a single, contin-
 343 uous fracture from tip-to-tip is a task that can face complications due to
 344 the presence of step-outs or edges that have degree-3 (or Y-nodes) on either
 345 ends. Such Y-Y motifs often form *step-outs* which impede continuous path
 346 finding as they may strike in a different direction as that of longer adjacent
 347 edges. They turn out to be bottlenecks when we seek to identify long and
 348 continuous paths using segment strike as a search attribute. Examples of
 349 such step-out edges are shown in Figs.12-13. To resolve the issue, we specifi-
 350 cally filter for graph edges that are below a certain length threshold that have
 351 a degree of 3 on both start and terminating ends. Below a certain length
 352 threshold corresponding to the resolution of the image, a *merge* operation
 353 can be carried out deleting the step-out and creating a degree-4 node (see
 354 Fig.12) after adding three edges and removing one node.

355 Above this length threshold, it is likely that the topology at either end of
 356 the step-out is correct, but the Y-Y edge needs to be *flattened* to correspond

357 with the strike angle of one pair of edges on either side (see Fig.13). In
 358 this case, merging of the step-out may incorrectly displace some edges of the
 359 spatial graph. In this procedure, the edges that are connected to the start
 360 and terminating nodes of each step-out are identified. A walk is identified
 361 for each of these edges. Though the step-out is a geometric feature that
 362 impedes the possibility of a walk, there are still possibilities of walks looking
 363 upstream on both directions away from the step-out. A decision is made
 364 as to which direction alongside the step-out provides the best increase in
 365 walkability. Once this is identified, the node of the step-out that causes
 366 the bottleneck is moved to a more preferable alignment. The sequence of
 367 graph manipulations involved in this flattening operation consists of adding
 368 three edges, removing three edges, adding one node and removing one node.
 369 The step-out flattening procedure therefore improves the walkability in one
 370 direction.

371 4.4.4. *Straightening fracture segments*

372 During piecewise polyline fitting as performed when vectorizing fracture
 373 traces (see Fig.6), a large number of points are inserted to represent the
 374 natural sinuosity of fracture traces. Within the graph representation these
 375 points are degree-2 nodes and are the predominant topology type. In terms
 376 of overall network topology, these nodes may not be very interesting, and
 377 hence it maybe useful to *straighten* or *flatten* the graph edges by removing
 378 these degree-2 nodes and replacing them by single edges between the non-
 379 degree 2 nodes. This type of graph manipulation involves removal of all
 380 edges that either start or end in degree-2 nodes (or both) and addition of
 381 single edges between the non-degree 2 nodes. The implementation of this

382 function is attached in the supplementary code. The effect of such an edge
383 straightening operation is depicted in Fig.14.

384 4.4.5. *From fracture traces to geologically significant fractures*

385 The geological identification of a fracture in the outcrop or from image
386 data is that of a discontinuity feature that is geometrically continuous with
387 the tip extremities either abutting another fracture, cutting across another
388 fracture, or terminating within rock matrix. In a typical manual interpretation,
389 the interpreter draws polylines in a digitizing software (eg. Adobe
390 Illustrator, Coreldraw, QGIS, ArcGIS etc) tracing across image pixels that
391 seemingly correspond to a perceived fracture using visual cues within the
392 image coupled with specific knowledge of the particular outcrop and general
393 training in structural geology. There are many ways in which such an interpretation
394 may be biased and lacking repeatability as discussed in Andrews
395 et al. (2019) and Peacock et al. (2019). Given these considerations, it is useful
396 to have an automated method of obtaining geologically significant fractures
397 (or fracture sets) rather than just fracture segments. A simple way to assign
398 segments to sets is to sort based on striking angles as is done in popular tools
399 such as FracPaQ (Healy et al., 2017), and NetworkGT (Nyberg et al., 2018);
400 however, this may be difficult when fractures are very sinuous.

401 The graph representation of a fracture network is complete when we have
402 list of nodes, spatial positioning data corresponding to each node, a list of
403 edges with start and terminating points indexed as per node numberings, and
404 a list of edge sequences to represent each fracture. Automatic tracing cannot
405 yield the edge sequences so that they represent sets of fractures (tip-to-tip).
406 To this end, a function is developed to automatically identify continuous

407 paths along graph edges based on twin rules of connectedness and small
 408 strike variation. The routine considers each edge individually and checks if
 409 adjacent edges fall within the threshold of edge strike, on either ends of the
 410 edge. Sequences of edges (or walks) are assigned as fractures. The routine
 411 is attached in the supplementary code. An example of a continuous and
 412 sinuous fracture automatically combined from graph segments are shown in
 413 Fig.15.

414 In a related publication based on the same dataset as ours, Passchier
 415 et al. (2021) manually interpret and classify continuous edges as belonging
 416 to a single generation. We have compared the results of the automated
 417 function described in this section to the manually assigned joint generations
 418 of Passchier et al. (2021) and there is generally a good agreement.

419 4.4.6. *Computing dual graphs*

420 A dual graph can be computed from a primal graph if the edges sequences
 421 corresponding to individual fractures (tip-to-tip) are known or is computed
 422 using function described in Section.4.4.5. The dual graph depicted in Fig.3,
 423 was computed from a shapefile in which fracture id's of manually interpreted
 424 fractures were already been listed. Given the edge sequence information,
 425 obtained either from manual interpretation or automatically, the procedure
 426 to compute the dual is by initializing an adjacency matrix whose size is equal
 427 to number of fractures (A_{adj} is an $n \times n$ matrix where 'n' is the number of
 428 tip-to-tip fractures). By parsing through the intersections made by each
 429 fracture with others, the sparse adjacency matrix is then built up by filling
 430 in rows and columns corresponding to fracture intersection. The function
 431 that accomplishes this is depicted in the supplementary code.

432 5. Results

433 The methods in Section.4 are applied to image tiles corresponding to
434 the five selected areas and based on these we generate five large networks.
435 The created fracture data are in the form of spatial graphs and shapefiles
436 attached in the supplementary data. A summary of the number of nodes,
437 edges, and tip-to-tip fractures (or walks) for each area is tabulated in Table.2.
438 Edge/node and edge/walk ratios are also shown as they give an indication as
439 to the connectedness of the networks. In order to illustrate the level of detail
440 within the generated network data, zoomed cut-out regions from Area 2 (
441 Figs.16-18) and Area 4 (Figs.19-21) are depicted. From the cut-outs of Area
442 2 in Figs.16-18, there are clear visual differences in fracturing even though
443 the orientations of fractures are quite consistent among all three samplings.
444 This is however, not the case in the cut-outs from Area 4 shown in Figs.19-21.
445 In Fig.19, a radial NW-SE trending fracture pattern that is orthogonally cut
446 by NE-SW fractures can be observed. The fracturing style is very different in
447 Fig.20 with a much more intense network. In Fig.20, the fracturing intensity
448 is highest with a much more complex pattern.

449 5.1. Length distributions and fracture set directions

450 Trace length distributions corresponding to the five areas are depicted in
451 Fig.22. Trace length distributions show the lengths from fracture tip-to-tip.
452 These are affected by boundaries of the sampled regions which may be ob-
453 served by comparing the plots of largest areas, 2 and 4, with the other three.
454 In Fig.23 we depict fractures plotted by their length classified into three bins
455 for Areas 1 & 3, which are stratigraphically the same layer. Similarly, the

length-binned fractures are depicted for Areas 2 & 4 in Fig.24 and for Area 5 in Fig.25.

The rose plots depicted in Fig.22 are computed from strike data that is a length-weighted average of the strike of edges that sum up to a tip-to-tip fracture. The rose plots highlight differences in fracture orientation between the layers. Orientation of the fractures do not vary significantly in Areas 1 & 3. However, Areas 2 & 4 from the same stratigraphic layer have considerably different fracture orientations. This is illustrated in Fig.24(b) with Area 4 containing curved and radial fractures. However, Area 2 does not have any curved fractures (see Fig.24(a)). Similar to Area 4, Area 5 also has curved fractures as can be seen in Fig.25. The scatter in rose-plots corresponding to Areas 4 & 5 is related to the presence of the curved joints.

From Fig.24 and Fig.25, spatial variations in the distribution of fractures in Areas 2,4, and 5 can be observed. The longest joints in Area 2 display a spatial variation with a larger concentration to the SW (see Fig.24(a)). In case of Area 4, the radial and curved fractures which are also the longest are located in the western part of Area 4 (see Fig.24(b)). The occurrence of these long, radial joints diminishes to the east of Area 4. In the case of Area 5, the long fractures has strikingly different curvature directions towards its east compared to its west (see Fig.25).

5.2. Network topological summary

From Manzocchi (2002), Sanderson & Nixon (2015), and others, an I-node corresponds to a fracture tip that is isolated, a Y-node is analogous to fracture tip that has abutting interactions with other fractures (or splaying fractures), and an X-node represents a fracture tip that cross-cuts another

481 fracture. The proportions of each node type can be summarized in an I-
482 Y-X ternary diagram. To quantify network topology, we use node degree
483 histograms instead of I-Y-X ternary plots. This is because of the need to
484 depict node degrees greater than four which are not unusual in large-scale
485 networks as is observed in the Lilstock pavement. Additionally, in the case
486 of dual graph representations, where fractures are represented as nodes, the
487 node degree can be larger. The node degree distribution of the primal graphs
488 corresponding to the five networks is depicted in Fig.26. These are plotted
489 in Fig.27. Degree distributions of all the primal graphs indicate that the
490 predominant node topology are Y-nodes with a 70-80 % contribution followed
491 by X-nodes.

492 The dual graph degree distributions provide insight into the connectivity
493 behaviour of each network. The topological summary of the dual graphs are
494 tabulated in Table.3. The node degree value indicates the number of connec-
495 tions that a fracture makes with other fractures within a network. Maximum
496 node degrees in dual graphs are observed from Areas 4 and 5 which contain
497 continuous and long, radial fractures. The correlation between dual graph
498 degree (number of intersections made a fracture) and the fracture length is
499 also plotted in Fig.27 depicting a positive correlation between fracture length
500 and number of intersections. The number of connections is least in Areas 1
501 and 3. This is possibly an effect of sample size as these regions are the
502 smallest and their spatial extent in the N-W direction is quite thin. Area 2,
503 despite covering more area than Area 5, has a lesser maximum dual degree.

504 5.3. Bounded area distribution

505 The fracture patterns develop and enclose bounded regions of unfractured
506 rocks. These enclosed polygonal areas are extracted from the spatial graphs
507 by identifying the primary cycles that are created by edges. The spatial
508 distribution of areas corresponding to these polygonal regions is depicted
509 in Fig.28 as a choropleth and depicts the variation across the layers. His-
510 tograms of the area distributions of each layer is depicted in Fig.29. Area
511 1 appears to have the largest block areas, followed by similar distributions
512 for Areas 3 and 5. The largest Areas 2 and 4 have smaller block areas with
513 visibly more intensive fracturing.

514 5.4. Spatial P_{20} and P_{21}

515 Fracture persistence measures (P_{ij}) formulated by Dershowitz & Herda
516 (1992) are used to investigate the spatial differences in fracturing. Within this
517 system, 'P' refers to persistence, the subscripts i and j indicate the dimen-
518 sionality of the fractured region considered and the fractures, respectively.
519 The fracture intensity, P_{21} and fracture density P_{20} metrics are computed
520 using the box-counting method by overlaying the networks with a cartesian
521 grid of box size of 2.5 x 2.5m. Fracture intensity (m/m^2) involves computing
522 2D trace length per area for each grid box. This is depicted for all areas in
523 Fig.30). Fracture density (m^{-2}) computes the number of segments within
524 each grid box and this is depicted in Fig.31. The persistence results reveals
525 regions within the outcrop with different fracturing motifs. Area 1 has the
526 least fracturing intensity and density which is uniform in the spatial distribu-
527 tion. Area 3 also is homogenous in the type of networks present. The greatest
528 variation is in Area 4 which has clear regions of low and high P_{21} and P_{20}

529 with a demarcable boundary. Area 2 has the most intense fracturing over all
530 regions is in the eastern parts of Area 2. Similar intense fracturing regions
531 can also be seen in the northern parts of Area 4. These are not fracture
532 corridors but progressively intense fracturing with smaller block areas.

533 6. Discussion

534 Manually tracing fracture networks from image data is time-consuming
535 and can introduce various types of biases depending upon skill, style, and per-
536 severance of the interpreter. These challenges are evident from the observed
537 networks in the structural geology literature which are not large and contin-
538 uous enough to study spatial network heterogeneity or do not have sufficient
539 resolution to correctly identify topology. Automatic tracing affords rapid
540 and unbiased network results which can be applied to large image datasets.
541 In case of the Lilstock pavement, high image resolution, enlarged apertures
542 due to erosion, high contrast in imagery between the wet apertures and dry
543 surface, and lack of vegetation, aided in easily applying automatic mapping.
544 One major drawback associated with automatic interpretations which pre-
545 cludes direct usability by a structural geologist and which were evident from
546 the results of Prabhakaran (2019) is that the detected segments were not yet
547 organized into geologically meaningful, tip-to-tip fractures.

548 The treatment of fracture networks as graph data structures with spatial
549 positioning allows us to perform various sequences of graph manipulations to
550 rectify these issues and convert the data into geologically realistic fractures.
551 The combined use of automatic tracing and application of such specific rou-
552 tines have resulted in a spectacular, large-scale fracture network dataset with

unprecedented spatial coverage and resolution. The network data is of great relevance as it can be used to obtain valuable insights into spatial arrangements of fracture networks and network morphogenesis. In this section, we delve into possible reasons for the observed spatial variations in network geomorphology. Issues regarding the applicability of automatic mapping and how large-scale network data can be leveraged are also considered.

6.1. *Spatial heterogeneity*

One of the interesting results of our fracture maps is the lateral differences in patterns. Areas 1 and 3 have relatively less spatial variation as can be quantified from spatial plots of fracturing intensity, density, and polygonal areas (see Fig.31, Fig.30, Fig.28). They are also the smallest regions with long and thin strips of exposed rock. Area 1 corresponds to regions with the least fracture intensity and density, and highest bounded areas. The most spatially extensive layer, comprising of Area 2 and 4 depict the most striking variations. From previous work by Gillespie et al., 2011; Rawnsley et al., 1998; Hancock & Engelder, 1989 and many others, the long radial, fan-like fracture sets are hydraulically-driven and originate from stress concentrations on the small fault. This region in the SE of Area 4 also has the least fracturing intensity with wide spacing between the radial fractures. The interference of small low-displacement faults can also be seen in the NE region of Area 2 which again has a low-fracture intensity. Similar to Area 4, Area 5 also contains highly sinuous fractures that can be linked to the NE trending regional fault. In Area 5, the long, radial fractures have strikingly different curvature directions towards its east as compared to its west (see Fig.25). These effects totally disappear in Areas 1,2, and 3 which have mostly straight fractures.

578 Within Area 2, a trend of high fracturing intensity can be observed towards
579 the SW which progressively decreases towards the NE. Area 5 has the largest
580 fracturing intensity in its centre and this progressively decreases to its east-
581 west peripheries. Passchier et al. (2021) highlighted spatial variations in the
582 presence of joints in the regions covered by Areas 2 and 4. From a total of
583 eight identified jointing generations, only two are distributed evenly across
584 both areas. Three sets of joints exclusively appear in Area 2 but are absent
585 in Area 4. Another three sets are found in both Areas 2 and 4, but they are
586 restricted to certain localized regions. The spatial variation of the polygonal
587 area distributions (Fig.28) follows a similar trend as the fracture persistence
588 plots (Fig.31 and Fig.30). The area distribution likely scales with thickness
589 of the limestone layers.

590 The reasons behind spatial variation may also originate from factors not
591 observable from simple photogrammetric data. For example, differences in
592 fracturing may emanate from local variations in layer thickness and due to
593 changes in mineralogical composition of the host-rock. Our image resolu-
594 tion does not include vein or stylolite networks which are also present in the
595 outcrop and whose spatial variation may have an influence on the develop-
596 ment and of the barren fracture networks that we have mapped. Spatial
597 layer thickness can be estimated by methods such as ground penetrating
598 radar (GPR) and mineralogical variation can be explored using UAV-based
599 sensors such as magnetic and hyperspectral imaging.

600 *6.2. From traces to timing*

601 Previous work on the Bristol Channel summarized in Section.3 have fo-
602 cussed on relationship between structural history of the region, exposed frac-

603 tures, and other large deformation features. Identifying fracture generations
604 and sequences of network evolution is routinely done based on geometric cri-
605 teria and topological relationships of fracture tips, sometimes supported by
606 geochemical analysis of cement within fractures. The problem of identifying
607 fracture timing from the automatically traced fractures was not in the scope
608 of this contribution. Using the same dataset as we have used, Passchier et al.
609 (2021) identified eight generations of fractures traced segments without re-
610 sorting to a fully detailed network interpretation. The oldest generations
611 were considered to be the most continuous and longest which do not abut
612 against others. Subsequent generations were then identified based on strike
613 and abutting criteria w.r.t each older joints generation. In their study, a cor-
614 relation between length and age seemed probable with only few exceptions.
615 In the same work, there are also highlighted cases where sequential rule-based
616 joint identification results in *Escherian* paradoxes. Another study by Wyller
617 (2019) focussed on an area that roughly conforms to the western parts of
618 Area 4 and was able to identify ten sets of joints using statistical analysis
619 of joint lengths, orientations, and topology. In this study as well, assigning
620 hierarchies based on abutting relations result in paradoxes which Procter &
621 Sanderson (2018) and Wyller (2019) refer to as *backcycling* between joint
622 generations.

623 The above studies are based on the assumption that abutting relation-
624 ships are a sufficient criteria, if not necessary, to be able to delineate fracture
625 sets into a hierarchy of fracturing episodes. Such approaches may not always
626 suffice, for instance, if fracturing drivers are due to high-deformation episodes
627 or there is evidence of complex structural inheritance. In outcrops such as

the Lilstock pavement, where fractures are mostly formed in low-deformation settings, simple geometric criteria as proposed by Passchier et al. (2021) may be programmed to automatically assign fractures into hierarchical episodes. Given large networks and well-defined criteria, it might be more prudent to use statistical strategies such as Markov chains to automatically assign generations (Snyder & Waldron, 2018). In future work, we intend to apply such automated approaches to the full-detailed fracture networks presented in this paper and compare the automatically-assigned generations to those that have been manually-assigned in previous literature relevant to the Lilstock pavement.

6.3. *Extent of applicability of automatic methods*

We have been able to extract a very large number of geologically relevant fracture traces focussing only on the opening-mode fractures that are visible from a flying altitude of 20-25 m. The quality of the interpretations are comparable to the work of a manual interpreter and this is attained in much less time (Weismüller et al., 2020). Often, the error in automatic tracing results are within the limits of subjectivity associated with even a well-trained interpreter. The largest variation in interpretation between manual and automatic is the creation of stepped-out segments. This is due to the fact that unlike manual interpretation where the interpreter can make a decision on a possible fracture intersection considering the full outcrop image, automatic methods make use of local information in the image which leads to uncertainty in regions which are more eroded than normal. The presence of step-outs sections was observed by Weismüller et al. (2020) when comparing topological differences between the two approaches and revealed that manual

653 interpretations result in topological distributions skewed to higher node de-
 654 grees. From a network connectivity point-of-view, such a configuration may
 655 be correct but this can result in shorter length distributions. This issue is not
 656 likely to arise in manual tracing as the interpreter uses multiple global cues
 657 available within an image to decide the continuity of a trace. We addressed
 658 these issues using the step-out fixing functions. The methods developed here
 659 are extendable to other photogrammetric datasets.

660 *6.4. Extension of outcrop fracture network data*

661 In subsurface applications, geomodelers often have to contend with sparse
 662 borehole fracture data as the only available ground-truth. Since geophys-
 663 ical imaging resolution are often too coarse to resolve subsurface fractures,
 664 outcropping fractures have long been considered as analogues to guide sub-
 665 surface discrete fracture network models. In a typical subsurface situation, it
 666 is required to be able to extrapolate away and interpolate between points of
 667 well control where fracture data exists in the form of cores, formation micro-
 668 images (FMI), and resistive / acoustic logging. This is a highly ill-posed
 669 problem as the naturally heterogeneous behaviour of fracture patterns are
 670 typically under-represented. This is due to inherent sampling bias within
 671 each well data point and well as uncertainty in relationship between large-
 672 scale geological drivers.

673 The commonly used methods for subsurface fracture network modelling
 674 are based on stochastic point processes that use 1D well data input such as
 675 fracture size, type, intensity, number of sets, and cumulative length distri-
 676 butions (Thovert et al., 2017). Stochastically-generated DFNs that utilize
 677 such sparse data to extrapolate, are often limited in their ability to represent

678 fracture clustering effects, spatial variations in fracture orientation, and topo-
 679 logical connections. Alternative methods to stochastic point-process based
 680 methods such as the semi-variogram approach of Hanke et al. (2018) applied
 681 to areal fracture intensity and fracture intersection density maps, and the
 682 multipoint statistics approach of (Bruna et al., 2019a,b) which use training
 683 images of user-defined outcrops can help in incorporating more geologically-
 684 realistic fracture networks into geological models. In this respect, one needs
 685 to assess the fracture network properties that are to be replicated and for
 686 which 2D fracture trace maps can provide additional value. From our analysis
 687 of the large-scale Lilstock fracture networks, we would suggest that DFN gen-
 688 erating methods should also be able to replicate bounded area distributions.
 689 This may be justified by the fact that fracture networks influence effective
 690 rock permeability also through time-dependent diffusive effects from the ma-
 691 trix. Since matrix block area distributions contributes to the matrix-fracture
 692 fluid exchange and it needs to be represented as a parameter. A second useful
 693 parameter that arises from 2D trace maps is the correlation between frac-
 694 ture length and number of intersections. From our analysis of dual graphs,
 695 (Fig.27) we find this to be positively-correlated. In the work of Andresen
 696 et al. (2013) and Vevatne et al. (2014) where fractures are represented using
 697 dual graphs, the networks display the property of *disassortativity* in which
 698 nodes of larger degree (longer fractures) share coordination with nodes of a
 699 smaller degree. This is also referred to as *small-world behaviour* (Watts &
 700 Strogatz, 1998), a property shared by many other classes of networks.

701 At this juncture, we revisit the point on applicability of outcrop-derived
 702 fracture networks. Recent work by Laubach et al. (2019) have raised ques-

tions on the use of fracture network data that has no provable correlation to subsurface fractures. Ukar et al. (2019) and Laubach et al. (2019) proposed protocols to identify suitable analogues based on vein networks rather than on barren fractures. In the case of network data presented in this article which are exclusively barren fractures, we repeat this caveat that though the data is useful in studying the fracture network properties and their spatial distribution, caution needs to be exerted when extrapolating to subsurface conditions.

7. Conclusion

We present automatically extracted, large-scale fracture networks from limestone pavements the Bristol Channel, UK using photogrammetric data previously published by Weismüller et al. (2020). The automatic extraction process is a combination of methods from Prabhakaran et al. (2019) and using programmatic routines described here. The functions developed receive fracture network input in the form of a graph data structure, perform node / edge manipulations on the graph so as to rectify issues such as lack of connectivity, artificial segmentation, and linking of segments. The resultant graphs can then be converted into geologically significant fracture traces amenable for further analysis. In summary, this contribution presents the following:

- fracture networks from five fractured limestone pavements spread over approximately 17,000 sq.m are automatically extracted using the complex shearlet transform method from UAV-borne photogrammetric imagery. From a spatial graph perspective, the number of fracture segments or edges is nearly 800,000. A set of programmatic functions is de-

727 signed to perform topological manipulations on fracture segments that
728 resolve discontinuities, artificial fragmentation, and combines the seg-
729 ments into geologically significant fractures. Depending upon thresh-
730 olds used, this results in around 350,000 fractures in total

- 731 • detailed quantification of networks using metrics such as fracture den-
732 sity, fracture intensity, node degree distributions, block area distribu-
733 tions, rose plots, and fracture length distributions are presented
- 734 • analysis of fracture networks in the different layers highlighting both
735 the intra-network and inter-network variability despite belonging to
736 similar stratigraphic layers
- 737 • analysis of node degree distributions indicating that the most common
738 topology type is the degree-3 node or Y-node indicating the sequential
739 development of the networks in each of the five studied outcrops with
740 younger and shorter fractures abutting on to older and longer fractures
- 741 • investigation of the relationship between degree distributions of dual
742 graphs and fracture lengths which reveals a strong positive correlation

743 **Declaration of Competing Interests** The authors declare that they
744 have no known competing financial interests or personal relationships that
745 could have appeared to influence the work reported in this paper.

746 **Acknowledgements** We would like to thank Quinten Boersma (TU Delft)
747 for his assistance with Digifract python scripts which were applied in
748 generating some plots in this article. Martijn Passchier (RWTH Aachen) is

749 thanked for sharing his manual interpretations and fracture generations in
750 the Lilstock outcrop.

751 **Code Availability**

- 752 1. The code used for automatic fracture detection is published as
753 supplement to Prabhakaran (2019) and is available to download from
754 the following GitHub repository:
755 [https://github.com/rahulprabhakaran/Automatic-Fracture-Detection-](https://github.com/rahulprabhakaran/Automatic-Fracture-Detection-Code/tree/v1.0.0)
756 [Code/tree/v1.0.0](https://github.com/rahulprabhakaran/Automatic-Fracture-Detection-Code/tree/v1.0.0) (last access: 30 March
757 2020)
- 758 2. The code to modify graphs is available from the following Github
759 repository:
760 <https://github.com/rahulprabhakaran/Fracture-Graphs/tree/v1.0.0>
761 (last access: 5 March 2021)

762 **Data Availability**

- 763 1. The fracture network data presented in this article is available in
764 shapefile, csv, and mat formats on the 4TU data repository associated
765 with this article (<https://doi.org/10.4121/14039234>).
- 766 2. The photogrammetric data of the Bristol Channel outcrop used in this
767 article is available at: <http://doi.org/10.18154/RWTH-2020-06903>

768 **Funding** JLU acknowledges support by the Deutsche
769 Forschungsgemeinschaft (DFG) (grant no. 316167043)

770 **Author Contributions** RP performed the automatic extraction of traces
771 from photogrammetric data, wrote the code to convert shapefiles to graphs
772 and graph modification functions, and wrote the manuscript with inputs

773 from all co-authors. CW acquired the UAV photogrammetric data at the
774 Lilstock outcrop, created the orthomosaics and tiling of images, and
775 contributed to the regional geology section of the manuscript. JU helped
776 acquire the UAV photogrammetric data at the Lilstock outcrop, initiated
777 and organised the collaborative efforts between the universities involved in
778 the project, discussed results, and helped in writing of the manuscript. GB
779 organised the collaboration for the Dutch part of the project, contributed
780 to the development of the methods, discussed the structure and discussion
781 of the results within the manuscript. DS provided funding and contributed
782 to discussions on the development of methods that are used in and not
783 limited to this manuscript.

784 **References**

- 785 Andresen, C., Hansen, A., Le Goc, R., Davy, P., & Hope, S.
786 (2013). Topology of fracture networks. *Frontiers in Physics*, 1, 7.
787 doi:10.3389/fphy.2013.00007.
- 788 Andrews, B. J., Roberts, J. J., Shipton, Z. K., Bigi, S., Tartarello, M. C., &
789 Johnson, G. (2019). How do we see fractures? quantifying subjective bias
790 in fracture data collection. *Solid Earth*, 10(2), 487–516. doi:10.5194/se-
791 10-487-2019.
- 792 Barthelemy, M. (2018). *Morphogenesis of Spatial Networks*. Lecture
793 Notes in Morphogenesis (2018th ed.). Springer International Publishing.
794 doi:10.1007/978-3-319-20565-6.
- 795 Bastian, M., Heymann, S., & Jacomy, M. (2009). Gephi: An open

796 source software for exploring and manipulating networks. URL:
797 <http://www.aaai.org/ocs/index.php/ICWSM/09/paper/view/154>.

798 Becker, S. P., Eichhubl, P., Laubach, S. E., Reed, R. M., Lander,
799 R. H., & Bodnar, R. J. (2010). A 48 m.y. history of fracture
800 opening, temperature, and fluid pressure: Cretaceous travis peak for-
801 mation, east texas basin. *GSA Bulletin*, 122, 1081–1093. URL:
802 <https://doi.org/10.1130/B30067.1>.

803 Belayneh, M. (2004). Palaeostress orientation inferred from surface mor-
804 phology of joints on the southern margin of the bristol channel basin,
805 uk. In *The Initiation, Propagation, and Arrest of Joints and Other*
806 *Fractures* 1 (pp. 243–255). Geological Society of London, Special Publi-
807 cations. URL: <https://sp.lyellcollection.org/content/231/1/243>.
808 doi:10.1144/GSL.SP.2004.231.01.14.

809 Belayneh, M., & Cosgrove, J. W. (2004). Fracture-pattern variations around
810 a major fold and their implications regarding fracture prediction using
811 limited data: an example from the bristol channel basin. In *The Initiation, Propagation, and Arrest of Joints and Other Fractures* (pp. 89–
812 102). Geological Society of London, Special Publications volume 231 (1).
813 doi:10.1144/GSL.SP.2004.231.01.06.

815 Belayneh, M., Geiger, S., & Matthai, S. K. (2006). Numerical simulation of
816 water injection into layered fractured carbonate reservoir analogs. *AAPG*
817 *Bulletin*, 90, 1473–1493. doi:10.1306/05090605153.

818 Bemis, S. P., Micklethwaite, S., Turner, D., James, M. R., Akciz, S., Thiele,

- 819 S. T., & Bangash, H. A. (2014). Ground-based and uav-based photogram-
820 metry: A multi-scale, high-resolution mapping tool for structural geol-
821 ogy and paleoseismology. *Journal of Structural Geology*, *69*, 163–178.
822 doi:10.1016/j.jsg.2014.10.007.
- 823 Berkowitz, B. (2002). Characterizing flow and transport in fractured geo-
824 logical media: A review. *Advances in Water Resources*, *25* (8), 861–884.
825 doi:10.1016/S0309-1708(02)00042-8.
- 826 Bertotti, G., Audra, P., Auler, A., Bezerra, F. H., de Hoop, S., Pontes, C.,
827 Prabhakaran, R., & Lima, R. (2020). The morro vermelho hypogenic karst
828 system (brazil): Stratigraphy, fractures, and flow in a carbonate strike-slip
829 fault zone with implications for carbonate reservoirs. *AAPG Bulletin*, *104*
830 (10), 2029–2050. doi:10.1306/05212019150.
- 831 Bisdom, K., Gauthier, B. D. M., Bertotti, G., & Hardebol, N. J.
832 (2014). Calibrating discrete fracture-network models with a carbonate
833 three-dimensional outcrop fracture network: Implications for naturally
834 fractured reservoir modeling. *AAPG Bulletin*, *98*, 1351–1376. URL:
835 <https://doi.org/10.1306/02031413060>. doi:10.1306/02031413060.
- 836 Bisdom, K., Nick, H., & Bertotti, G. (2017). An integrated workflow for
837 stress and flow modelling using outcrop-derived discrete fracture networks.
838 *Computers & Geosciences*, *103*, 21–35. doi:10.1016/j.cageo.2017.02.019.
- 839 Boersma, Q., Prabhakaran, R., Bezerra, F. H., & Bertotti, G. (2019). Link-
840 ing natural fractures to karst cave development: a case study combining

841 drone imagery, a natural cave network and numerical modelling. *Petroleum*
842 *Geoscience*, 25, 454–469. doi:10.1144/petgeo2018-151.

843 Bourne, S., & Willemse, E. (2001). Elastic stress control on the pattern of
844 tensile fracturing around a small fault network at nash point, uk. *Journal of*
845 *Structural Geology*, 23 (11), 1753–1770. doi:10.1016/S0191-8141(01)00027-
846 X.

847 Brooks, M., Trayner, P. M., & Trimble, T. J. (1988). Mesozoic reactivation of
848 variscan thrusting in the bristol channel area, uk. *Journal of the Geological*
849 *Society*, 145 (3), 439–444. doi:10.1144/gsjgs.145.3.0439.

850 Bruna, P., Prabhakaran, R., Bertotti, G., Straubhaar, J., Plateaux, R.,
851 Maerten, L., Mariethoz, G., & Meda, M. (2019a). The mps-based
852 fracture network simulation method: Application to subsurface do-
853 main. *81st EAGE Conference and Exhibition, London 2019, 2019*, 1–5.
854 doi:10.3997/2214-4609.201901679.

855 Bruna, P.-O., Straubhaar, J., Prabhakaran, R., Bertotti, G., Bisdom, K.,
856 Mariethoz, G., & Meda, M. (2019b). A new methodology to train fracture
857 network simulation using multiple-point statistics. *Solid Earth*, 10 (2),
858 537–559. doi:10.5194/se-10-537-2019.

859 Csardi, G., & Nepusz, T. (2006). The igraph software package for com-
860 plex network research. *InterJournal, Complex Systems*, 1695. URL:
861 <https://igraph.org>.

862 Dart, C. J., McClay, K., & Hollings, P. N. (1995). 3d analysis
863 of inverted extensional fault systems, southern bristol channel basin,

uk. *Geological Society, London, Special Publications*, 88 (1), 393–413.
doi:10.1144/GSL.SP.1995.088.01.21.

De Berg, M., Van Kreveld, M., Overmars, M., & Schwarzkopf, O. C. (2000).
Computational Geometry. Algorithms and Applications. Springer, Berlin,
Heidelberg. doi:10.1007/978-3-662-04245-8.

Dershowitz, W. S., & Herda, H. H. (1992). Interpretation of fracture spacing
and intensity. URL: <https://doi.org/>.

Engelder, T., & Peacock, D. C. (2001). Joint development normal to re-
gional compression during flexural-flow folding: the lilstock buttress anti-
cline, somerset, england. *Journal of Structural Geology*, 23 (2), 259–277.
doi:10.1016/S0191-8141(00)00095-X.

Gillespie, P., Monsen, E., Maerten, L., Hunt, D., Thurmond,
J., & Tuck, D. (2011). Fractures in Carbonates: From Dig-
ital Outcrops to Mechanical Models. In *Outcrops Revitalized:
Tools, Techniques and Applications*. SEPM Society for Sedimen-
tary Geology. URL: <https://doi.org/10.2110/sepmcsp.10.137>.
doi:10.2110/sepmcsp.10.137.

Glen, R., Hancock, P., & Whittaker, A. (2005). Basin inversion by
distributed deformation: the southern margin of the bristol channel
basin, england. *Journal of Structural Geology*, 27 (12), 2113–2134.
doi:10.1016/j.jsg.2005.08.006.

Guo, L., Latham, J.-P., & Xiang, J. (2017). A numerical study
of fracture spacing and through-going fracture formation in layered

- 887 rocks. *International Journal of Solids and Structures*, 110-111, 44–57.
888 doi:10.1016/j.ijsolstr.2017.02.004.
- 889 Hagberg, A. A., Schult, D. A., & Swart, P. J. (2008). Exploring network
890 structure, dynamics, and function using networkx. In G. Varoquaux,
891 T. Vaught, & J. Millman (Eds.), *Proceedings of the 7th Python in Sci-*
892 *ence Conference* (pp. 11 – 15). Pasadena, CA USA.
- 893 Hancock, P., & Engelder, T. (1989). Neotectonic joints. *GSA Bulletin*, 101
894 (10), 1197–1208. doi:10.1130/0016-7606(1989)101;1197:NJ;2.3.CO;2.
- 895 Hanke, J. R., Fischer, M. P., & Pollyea, R. M. (2018). Directional semivar-
896 iogram analysis to identify and rank controls on the spatial variability
897 of fracture networks. *Journal of Structural Geology*, 108, 34 – 51. URL:
898 <http://www.sciencedirect.com/science/article/pii/S0191814117302699>.
899 doi:<https://doi.org/10.1016/j.jsg.2017.11.012>. Spatial arrangement of frac-
900 tures and faults.
- 901 Healy, D., Rizzo, R. E., Cornwell, D. G., Farrell, N. J., Watkins,
902 H., Timms, N. E., Gomez-Rivas, E., & Smith, M. (2017).
903 Fracpaq: A matlabTM toolbox for the quantification of frac-
904 ture patterns. *Journal of Structural Geology*, 95, 1 – 16. URL:
905 <http://www.sciencedirect.com/science/article/pii/S0191814116302073>.
906 doi:<https://doi.org/10.1016/j.jsg.2016.12.003>.
- 907 Hodgetts, D. (2013). Laser scanning and digital outcrop geology in the
908 petroleum industry: A review. *Marine and Petroleum Geology*, 46, 335–
909 354. doi:10.1016/j.marpetgeo.2013.02.014.

- 910 Kelly, P., Peacock, D., Sanderson, D., & McGurk, A. (1999). Selective
 911 reverse-reactivation of normal faults, and deformation around reverse-
 912 reactivated faults in the mesozoic of the somerset coast. *Journal of Struc-*
 913 *tural Geology*, 21 (5), 493–509. doi:10.1016/S0191-8141(99)00041-3.
- 914 Laubach, S. E., Fall, A., Copley, L. K., Marrett, R., & Wilkins, S. J. (2016).
 915 Fracture porosity creation and persistence in a basement-involved laramide
 916 fold, upper cretaceous frontier formation, green river basin, usa. *Geological*
 917 *Magazine*, 153, 887–910. doi:10.1017/S0016756816000157.
- 918 Laubach, S. E., Lander, R. H., Criscenti, L. J., Anovitz, L. M., Urai, J. L.,
 919 Pollyea, R. M., Hooker, J. N., Narr, W., Evans, M. A., Kerisit, S. N.,
 920 Olson, J. E., Dewers, T., Fisher, D., Bodnar, R., Evans, B., Dove, P.,
 921 Bonnell, L. M., Marder, M. P., & Pyrak-Nolte, L. (2019). The role of
 922 chemistry in fracture pattern development and opportunities to advance
 923 interpretations of geological materials. *Reviews of Geophysics*, 57, 1065–
 924 1111. doi:10.1029/2019RG000671.
- 925 Lavoine, E., Davy, P., Darcel, C., & Munier, R. (2020). A discrete
 926 fracture network model with stress-driven nucleation: Impact on clus-
 927 tering, connectivity, and topology. *Frontiers in Physics*, 8, 9. URL:
 928 <https://www.frontiersin.org/article/10.3389/fphy.2020.00009>.
 929 doi:10.3389/fphy.2020.00009.
- 930 Lepillier, B., Yoshioka, K., Parisio, F., Bakker, R., & Bruhn, D.
 931 (2020). Variational phase-field modeling of hydraulic fracture interac-
 932 tion with natural fractures and application to enhanced geothermal sys-

- 933 tems. *Journal of Geophysical Research: Solid Earth*, 125, e2020JB019856.
934 doi:10.1029/2020JB019856.
- 935 Loosveld, R. J. H., & Franssen, R. C. M. W. (1992). Extensional
936 vs. shear fractures: Implications for reservoir characterisation. In
937 *European Petroleum Conference, Cannes, France* (p. 8). European
938 Petroleum Conference, Cannes, France Society of Petroleum Engineers.
939 doi:10.2118/25017-MS.
- 940 Manzocchi, T. (2002). The connectivity of two-dimensional networks of
941 spatially correlated fractures. *Water Resources Research*, 38, 1–1–1–20.
942 doi:10.1029/2000WR000180.
- 943 National Research Council (1996). *Rock Fractures and Fluid Flow: Contem-*
944 *porary Understanding and Applications, Washington, DC*. (1996th ed.).
945 Washington, DC: The National Academies Press. doi:10.17226/2309.
- 946 Nemčok, M., Gayer, R., & Milorizos, M. (1995). Structural analysis of the
947 inverted bristol channel basin: implications for the geometry and timing
948 of fracture porosity. In *Basin Inversion* (pp. 355–392). The Geological
949 Society, London volume 88. doi:10.1144/GSL.SP.1995.088.01.20.
- 950 Nishizeki, T., & Rahman, M. (2004). *Planar Graph*
951 *Drawing*. World Scientific Publishing. URL:
952 <https://www.worldscientific.com/doi/abs/10.1142/5648>.
953 doi:10.1142/5648.
- 954 Nyberg, B., Nixon, C. W., & Sanderson, D. J. (2018). NetworkGT: A GIS

955 tool for geometric and topological analysis of two-dimensional fracture net-
956 works. *Geosphere*, 14, 1618–1634. doi:10.1130/GES01595.1.

957 Olson, J. E. (2004). Predicting fracture swarms — the influence of sub-
958 critical crack growth and the crack-tip process zone on joint spacing
959 in rock. *Geological Society, London, Special Publications*, 231, 73–88.
960 doi:10.1144/GSL.SP.2004.231.01.05.

961 Olson, J. E., Laubach, S. E., & Lander, R. H. (2009). Natural fracture char-
962 acterization in tight gas sandstones: Integrating mechanics and diagenesis.
963 *AAPG Bulletin*, 93 (11), 1535–1549. doi:10.1306/08110909100.

964 Palamakumbura, R., Krabbendam, M., Whitbread, K., & Arn-
965 hardt, C. (2020). Data acquisition by digitizing 2-d fracture net-
966 works and topographic lineaments in geographic information sys-
967 tems: further development and applications. *Solid Earth*, 11, 1731–
968 1746. URL: <https://se.copernicus.org/articles/11/1731/2020/>.
969 doi:10.5194/se-11-1731-2020.

970 Passchier, M., Passchier, C., Weismüller, C., & Urai, J. (2021). The joint
971 sets on the lilstock benches, uk. observations based on mapping a full res-
972 olution uav-based image. *Journal of Structural Geology preprint, preprint*.
973 doi:10.31223/X5R01M.

974 Peacock, D., Sanderson, D., Bastesen, E., Rotevatn, A., & Storstein, T.
975 (2019). Causes of bias and uncertainty in fracture network analysis. *Nor-
976 wegian Journal of Geology*, 99(1). doi:10.17850/njg99-1-06.

- 977 Peacock, D. C. P. (2004). Differences between veins and joints us-
 978 ing the example of the jurassic limestones of somerset. In *The Ini-*
 979 *tiation, Propagation, and Arrest of Joints and Other Fractures* (pp.
 980 209–221). Geological Society of London, Special Publications volume
 981 231. URL: <https://sp.lyellcollection.org/content/231/1/209>.
 982 doi:10.1144/GSL.SP.2004.231.01.12.
- 983 Prabhakaran, R. (2019). rahulprabhakaran/Automatic-Fracture-
 984 Detection- Code(supplement to Solid Earth Manuscript se-2019-104).
 985 doi:10.5281/zenodo.3245452.
- 986 Prabhakaran, R., Bruna, P.-O., Bertotti, G., & Smeulders, D. (2019). An
 987 automated fracture trace detection technique using the complex shearlet
 988 transform. *Solid Earth*, 10 (6), 2137–2166. doi:10.5194/se-10-2137-2019.
- 989 Procter, A., & Sanderson, D. J. (2018). Spatial and layer-controlled vari-
 990 ability in fracture networks. *Journal of Structural Geology*, 108, 52–65.
 991 doi:10.1016/j.jsg.2017.07.008. Spatial arrangement of fractures and faults.
- 992 Rawnsley, K., Peacock, D., Rives, T., & Petit, J.-P. (1998). Joints in the
 993 mesozoic sediments around the bristol channel basin. *Journal of Structural*
 994 *Geology*, 20 (12), 1641–1661. doi:10.1016/S0191-8141(98)00070-4.
- 995 Reisenhofer, R., Kiefer, J., & King, E. J. (2016). Shearlet-based detection of
 996 flame fronts. *Experiments in Fluids*, 57, 41. doi:10.1007/s00348-016-2128-
 997 6.
- 998 Remij, E. W., Remmers, J. J. C., Pizzocolo, F., Smeulders, D. M. J., &
 999 Huyghe, J. M. (2015). A partition of unity-based model for crack nucleation

1000 and propagation in porous media, including orthotropic materials. *Trans-*
1001 *port in Porous Media*, 106 (3), 505–522. doi:10.1007/s11242-014-0399-z.

1002 Sanderson, D. J., & Nixon, C. W. (2015). The use of topology in frac-
1003 ture network characterization. *Journal of Structural Geology*, 72, 55–66.
1004 doi:10.1016/j.jsg.2015.01.005.

1005 Sanderson, D. J., Peacock, D. C., Nixon, C. W., & Rotevatn, A. (2019).
1006 Graph theory and the analysis of fracture networks. *Journal of Structural*
1007 *Geology*, 125, 155–165. doi:10.1016/j.jsg.2018.04.011. Back to the future.

1008 Santiago, E., Velasco-Hernández, J. X., & Romero-Salcedo, M. (2016).
1009 A descriptive study of fracture networks in rocks using com-
1010 plex network metrics. *Computers and Geosciences*, 88, 97–114.
1011 doi:10.1016/j.cageo.2015.12.021.

1012 Scott, D. N., & Wohl, E. E. (2019). Bedrock fracture influences on geomor-
1013 phic process and form across process domains and scales. *Earth Surface*
1014 *Processes and Landforms*, 44 (1), 27–45. doi:10.1002/esp.4473.

1015 Snyder, M. E., & Waldron, J. W. (2018). Fracture overprinting history
1016 using markov chain analysis: Windsor-kennetcook subbasin, mar-
1017 itimes basin, canada. *Journal of Structural Geology*, 108, 80 – 93. URL:
1018 <http://www.sciencedirect.com/science/article/pii/S0191814117301505>.
1019 doi:<https://doi.org/10.1016/j.jsg.2017.07.009>. Spatial arrangement of frac-
1020 tures and faults.

1021 Spruženiece, L., Späth, M., Urai, J. L., Ukar, E., Selzer, M., Nestler, B.,
1022 & Schwedt, A. (2020). Formation of wide-blocky calcite veins by ex-

1023 trement growth competition. *Journal of the Geological Society*, . URL:
1024 <https://doi.org/10.1144/jgs2020-104>.

1025 Thomas, R. N., Paluszny, A., & Zimmerman, R. W. (2018). Effect of
1026 fracture growth velocity exponent on fluid flow through geomechanically-
1027 grown 3d fracture networks. In *2nd International Discrete Fracture*
1028 *Network Engineering Conference, 20-22 June 2018, Seattle, Washing-*
1029 *ton, USA*. Seattle, Washington, USA: ARMA-DFNE-18-0239. URL:
1030 <https://www.onepetro.org/conference-paper/ARMA-DFNE-18-0239>.

1031 Thomas, R. N., Paluszny, A., & Zimmerman, R. W. (2020). Growth of
1032 three-dimensional fractures, arrays, and networks in brittle rocks un-
1033 der tension and compression. *Computers and Geotechnics*, *121*, 103447.
1034 doi:10.1016/j.compgeo.2020.103447.

1035 Thovert, J.-F., Mourzenko, V., & Adler, P. (2017). Percolation in three-
1036 dimensional fracture networks for arbitrary size and shape distributions.
1037 *Physical Review E*, *95* (4), 042112. doi:10.1103/PhysRevE.95.042112.

1038 Ukar, E., Laubach, S. E., & Hooker, J. N. (2019). Outcrops as
1039 guides to subsurface natural fractures: Example from the nikanassin
1040 formation tight-gas sandstone, grande cache, alberta foothills,
1041 canada. *Marine and Petroleum Geology*, *103*, 255–275. URL:
1042 <http://www.sciencedirect.com/science/article/pii/S0264817219300492>.

1043 Valentini, L., Perugini, D., & Poli, G. (2007a). The ‘small-world’
1044 nature of fracture/conduit networks: Possible implications for dise-
1045 quilibrium transport of magmas beneath mid-ocean ridges. *Jour-*

1046 *Journal of Volcanology and Geothermal Research*, 159 (4), 355–365.
1047 doi:10.1016/j.jvolgeores.2006.08.002.

1048 Valentini, L., Perugini, D., & Poli, G. (2007b). The “small-world” topol-
1049 ogy of rock fracture networks. *Physica A: Statistical Mechanics and its*
1050 *Applications*, 377 (1), 323–328. doi:10.1016/j.physa.2006.11.025.

1051 Valliappan, V., Remmers, J. J. C., Barnhoorn, A., & Smeulders, D. M. J.
1052 (2019). A numerical study on the effect of anisotropy on hydraulic
1053 fractures. *Rock Mechanics and Rock Engineering*, 52, 591–609. URL:
1054 <https://doi.org/10.1007/s00603-017-1362-4>.

1055 Vevatne, J. N., Rimstad, E., Hope, S. M., Korsnes, R., & Hansen, A.
1056 (2014). Fracture networks in sea ice. *Frontiers in Physics*, 2, 21. URL:
1057 <https://www.frontiersin.org/article/10.3389/fphy.2014.00021>.
1058 doi:10.3389/fphy.2014.00021.

1059 Virgo, S., Abe, S., & Urai, J. L. (2016). The influence of load-
1060 ing conditions on fracture initiation, propagation, and interaction in
1061 rocks with veins: Results from a comparative discrete element method
1062 study. *Journal of Geophysical Research: Solid Earth*, 121, 1730–1738.
1063 doi:10.1002/2016JB012792.

1064 Watts, D. J., & Strogatz, S. H. (1998). Collective dynam-
1065 ics of ‘small-world’ networks. *Nature*, 393, 440–442. URL:
1066 <https://doi.org/10.1038/30918>.

1067 Weismüller, C., Passchier, M., Urai, J., & Reicherter, K. (2020). The fracture
1068 network in the lilstock pavement, bristol channel, uk: digital elevation

1069 models and orthorectified mosaics created from unmanned aerial vehicle
1070 imagery. *RWTH Publications*, . doi:10.18154/RWTH-2020-06903.

1071 Weismüller, C., Prabhakaran, R., Passchier, M., Urai, J. L., Bertotti, G.,
1072 & Reicherter, K. (2020). Mapping the fracture network in the lilstock
1073 pavement, bristol channel, uk: manual versus automatic. *Solid Earth*, 11
1074 (5), 1773–1802. doi:10.5194/se-11-1773-2020.

1075 Welch, M. J., Luthje, M., & Glad, A. C. (2019). Influence of
1076 fracture nucleation and propagation rates on fracture geometry: in-
1077 sights from geomechanical modelling. *Petroleum Geoscience*, 25,
1078 470–489. URL: <https://pg.lyellcollection.org/content/25/4/470>.
1079 doi:10.1144/petgeo2018-161.

1080 Wyller, F. A. (2019). Spatio-temporal development of a joint network and
1081 its properties: a case study from lilstock, uk.

1082 Yoshioka, K., & Bourdin, B. (2016). A variational hydraulic fracturing model
1083 coupled to a reservoir simulator. *International Journal of Rock Mechanics
1084 and Mining Sciences*, 88, 137–150. doi:10.1016/j.ijrmms.2016.07.020.

Table 1: Study areas and approximate area covered

Region	Image tiles	Approx. area (sq.m)
Area 1	58	2034
Area 2	128	6017
Area 3	25	714
Area 4	107	6749
Area 5	34	1473

Table 2: Summary of primal graph structure

Region	Edges (e)	Nodes (n)	e/n	Walks (w)	e/w	Polygons
Area 1	42301	30299	1.39	18078	2.34	11992
Area 2	364703	228661	1.59	123592	2.95	136053
Area 3	40243	26372	1.52	16900	2.38	13874
Area 4	365333	235089	1.55	141344	2.58	129690
Area 5	78151	49771	1.57	28892	2.7	27220

Table 3: Summary of dual graph structure

Region	Nodes (n)	Edges(e)	e/n	Max degree
Area 1	18078	34077	1.88	65
Area 2	124006	301077	2.42	177
Area 3	16900	36320	2.14	73
Area 4	141344	314537	5.27	347
Area 5	28892	65867	2.28	236

Table 4: Summary of primal graph edges based on topology

Edge type	Area 1	Area 2	Area 3	Area 4	Area 5
1-1		4			
1-3	4041	7048	1007	5127	783
1-4	139	552	12	87	43
1-5	3	27	1		8
1-6		7		1	
3-3	30612	176360	27186	238130	47983
3-4	6815	127218	10355	99922	23793
3-5	182	13740	386	4902	1610
3-6	5	1708	18	329	83
3-7		141	6	23	
3-8		9			
4-4	478	30074	1161	15094	3327
4-5	25	6328	100	1522	465
4-6	1	884	6	129	29
4-7		63	1	4	
4-8		7			
5-5		392	4	53	25
5-6		115		9	2
5-7		11		1	
6-6		13			
6-7		2			
Total	42301	364703	40243	365333	78151

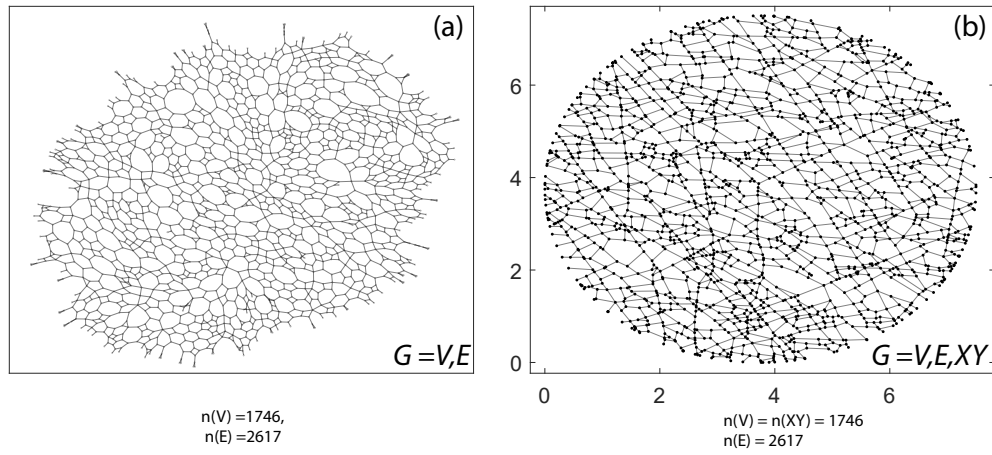


Figure 1: (a) A graph with no spatial positioning can be simply depicted as nodes and edges with a method of planar drawing (Nishizeki & Rahman, 2004). Here a fracture network is converted to a graph and drawn in a "gravity" layout. (b) The fracture graph with spatial positioning applied to each of its nodes (dimensions in metres).

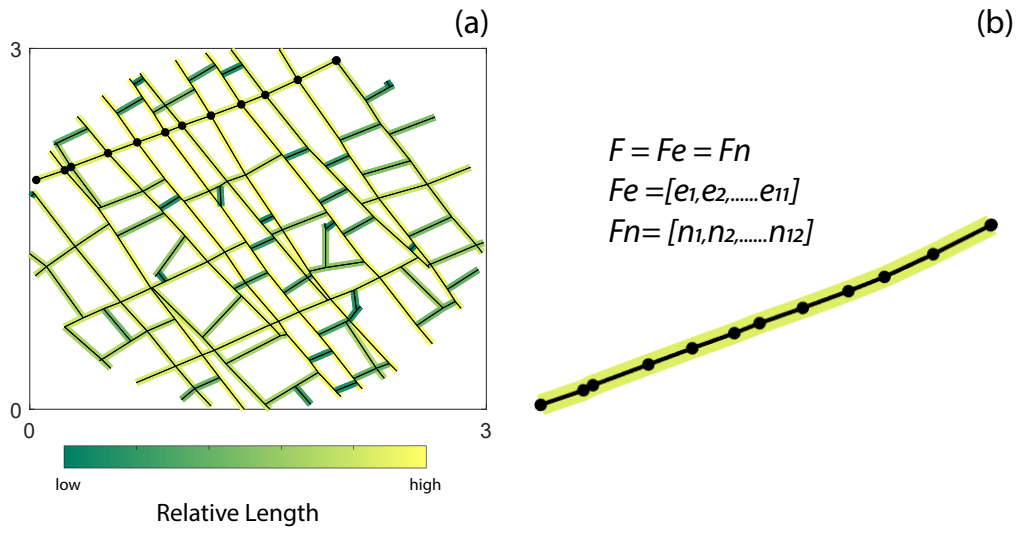


Figure 2: (a) An example of a fracture network plotted as a spatial graph with individual fractures from tip-to-tip colour coded based on fracture length (dimensions in metres). One fracture is highlighted with enlarged nodes (b) enlarged view of a single fracture F within a spatial graph, defined as a set of ' m ' edges or ' $n = m + 1$ ' nodes

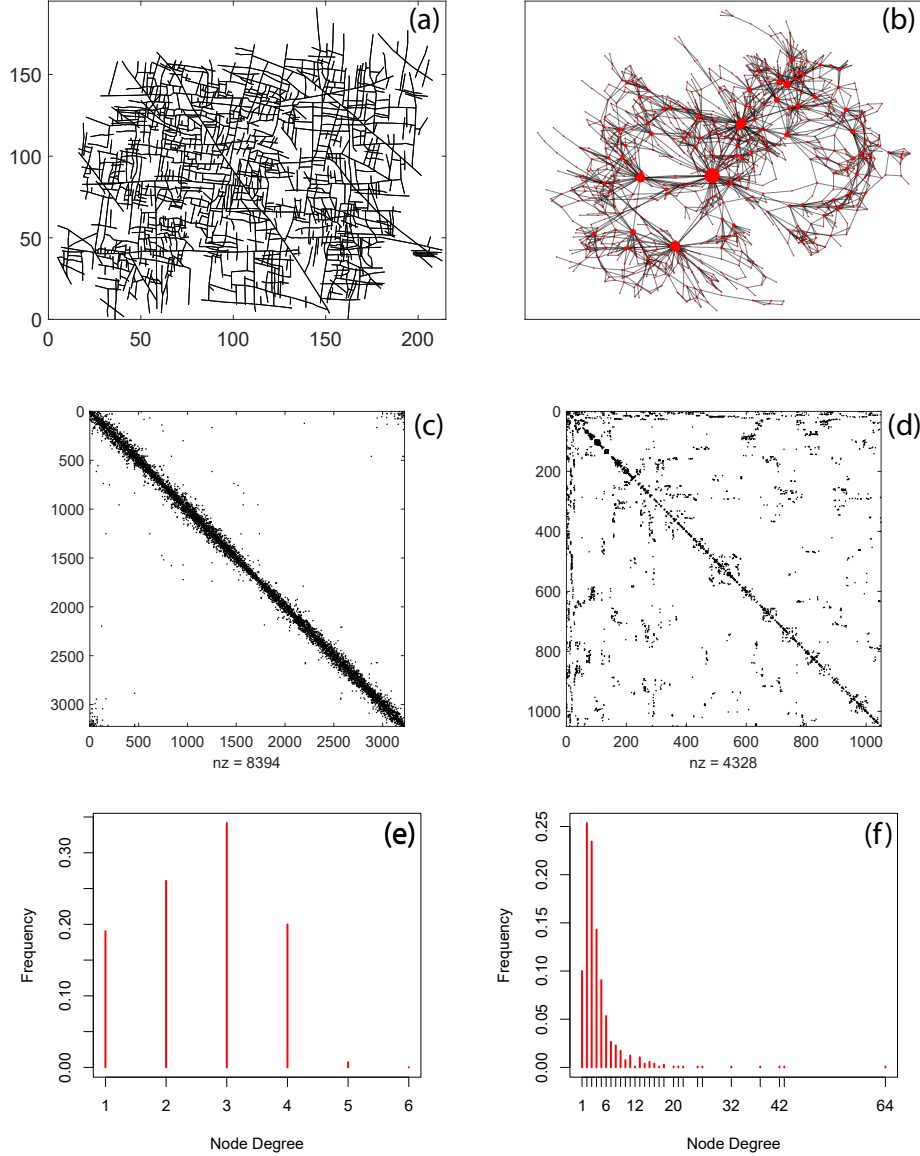


Figure 3: (a) Primal graph representation of a manually interpreted fracture network, Apodi-4, from Bisdom et al. (2017) in the Jandaira formation of the Potiguar Basin, Brazil having 3309 nodes and 4258 edges. Only the largest connected component of the network is depicted after removing all isolated fractures. (b) Dual graph representation of the Apodi-4 fracture network using a 'force' layout. Fracture traces from tip-to-tip are represented as graph nodes and intersections between fractures are considered as edges. The dual representations has 2172 edges and 1082 nodes. Node size is plotted proportional to the node degrees and highlights the centrality of the relatively few long fractures (c) Adjacency matrix of primal graph (d) Adjacency matrix of dual graph (e) Degree histogram representing node topology of primal graph (f) Degree histogram representing node topology of dual graph



Figure 4: Overview of the study area located at Listock, Bristol Channel, UK generated from UAV photogrammetry at an altitude of 100 m. The orthomosaic is available as a dataset (Weismüller et al., 2020). Shapefiles of UK regional boundaries used in this image is obtained from <https://geoportal.statistics.gov.uk/> available under an Open Government Licence v3.0.

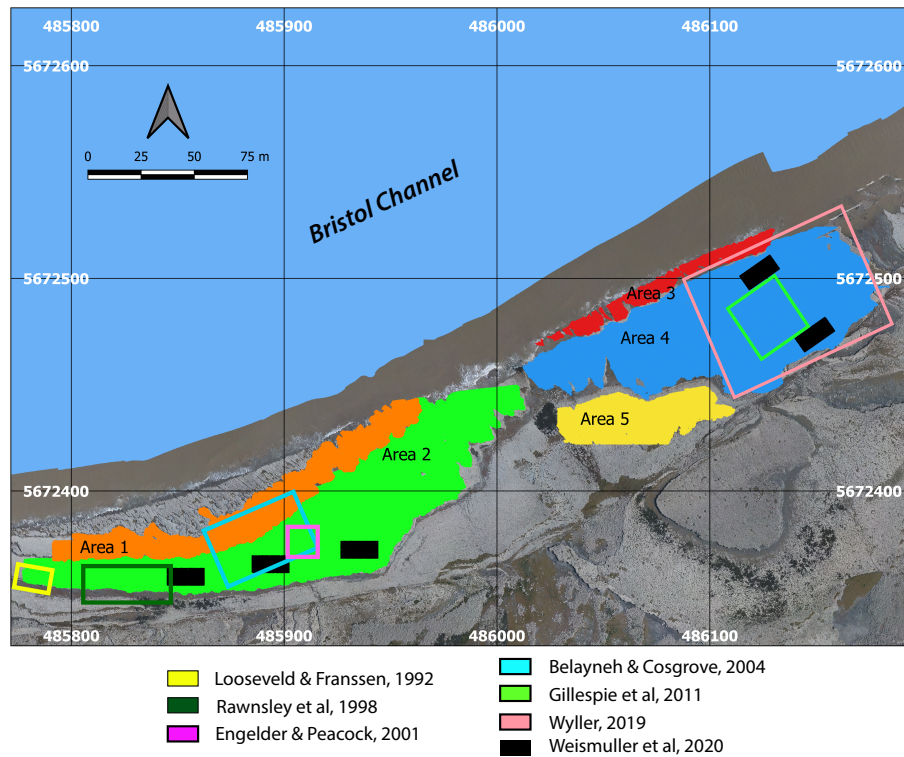


Figure 5: Overview of the spatial extent of the five areas within the Bristol Channel outcrop where fracture networks are automatically extracted. Approximate areas where previous studies done within the same outcrop are also highlighted.

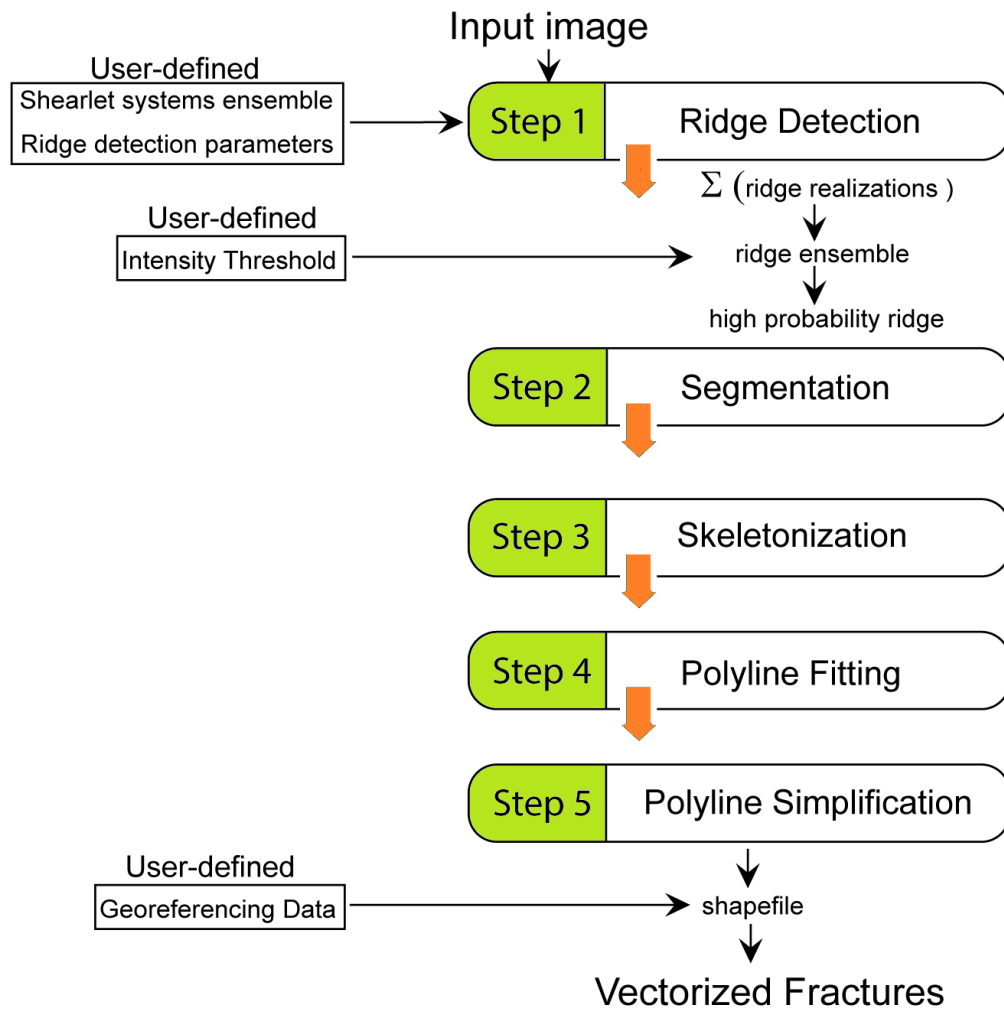


Figure 6: Automatic detection workflow used to convert UAV photogrammetric images to fracture traces used previously in Prabhakaran (2019) and Weismüller et al. (2020).

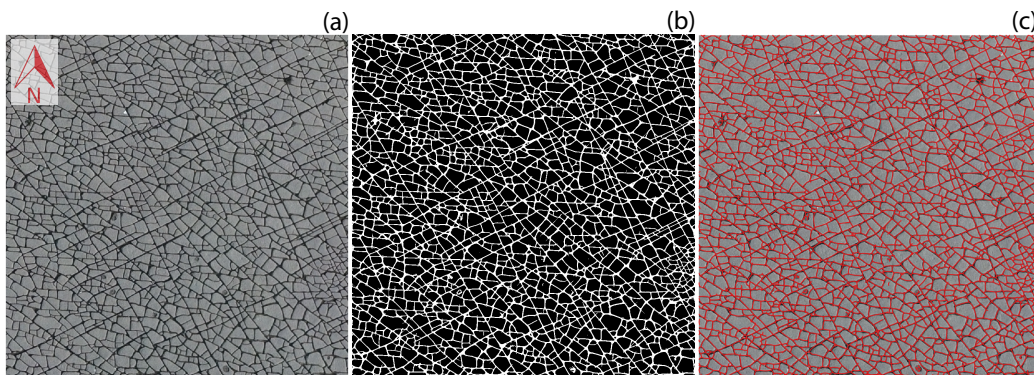


Figure 7: (a) An image tile (9.3 x 9.3 m) from the Bristol Channel dataset (b) computed ridge ensemble (c) the vectorized shapefile overlain on the image

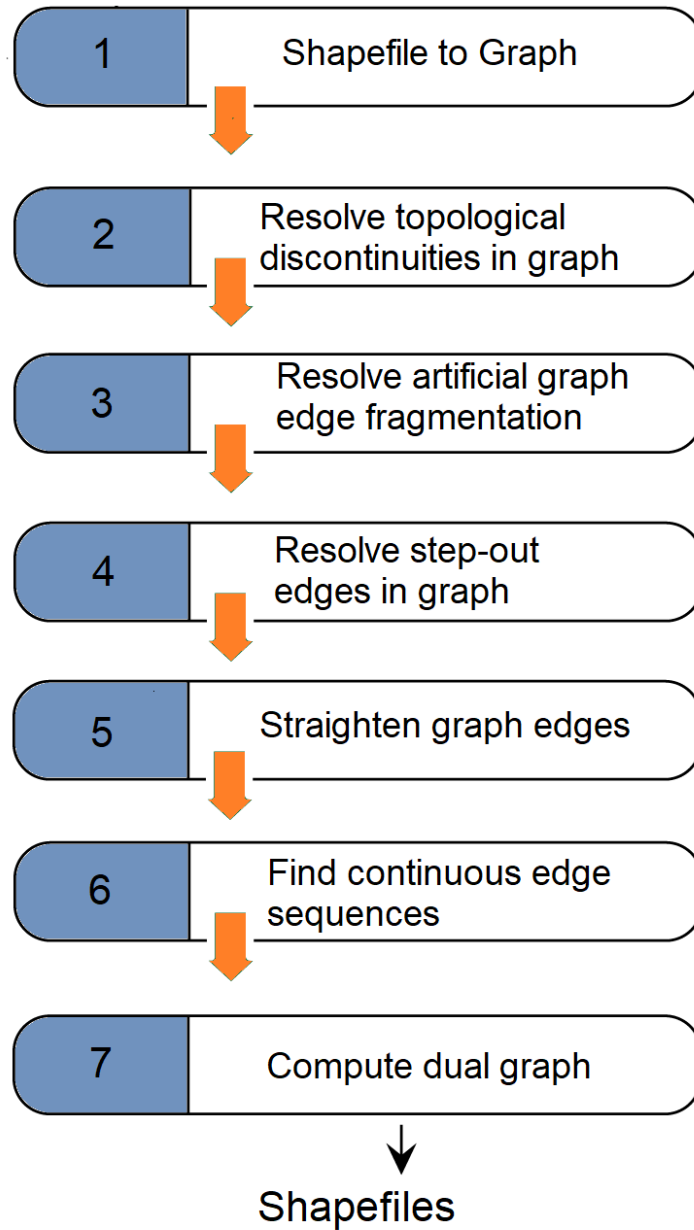


Figure 8: Sequence of graph manipulation routines to convert shapefiles of automatically traced fracture segments to geologically significant fracture traces and dual graph representations.

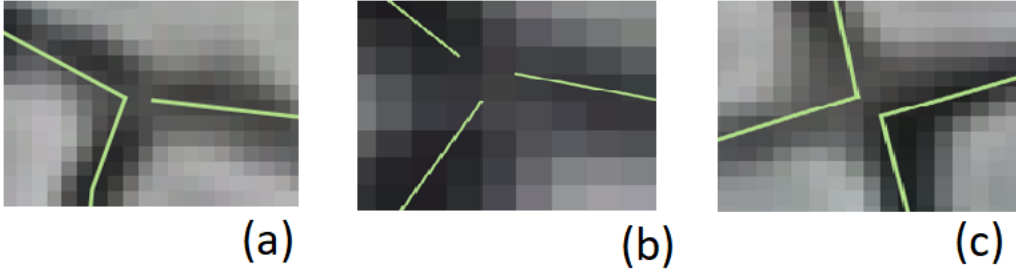


Figure 9: Common topological errors caused by automatic detection (a) a degree-3 connection inaccurately traced as a degree-2 node with two nearly orthogonal edges in close proximity to a degree-1 node (b) a degree-3 connection incorrectly traced as three degree-1 nodes in close proximity (c) two degree-2 nodes with nearly orthogonal edges that are disconnected

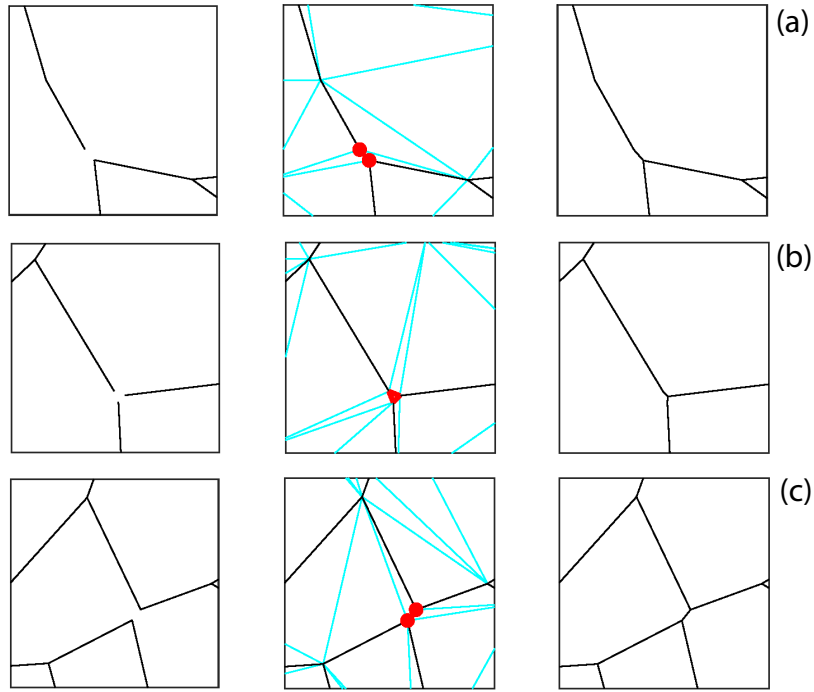


Figure 10: Detail of rectification of the three types of topological discontinuities (a) type-1 discontinuity with degree-1 node in close proximity to a sharp-angled degree-node (b) type-2 discontinuity with three degree-1 nodes in close proximity (c) type-3 discontinuity with two degree-2 nodes having sharp angles in close proximity

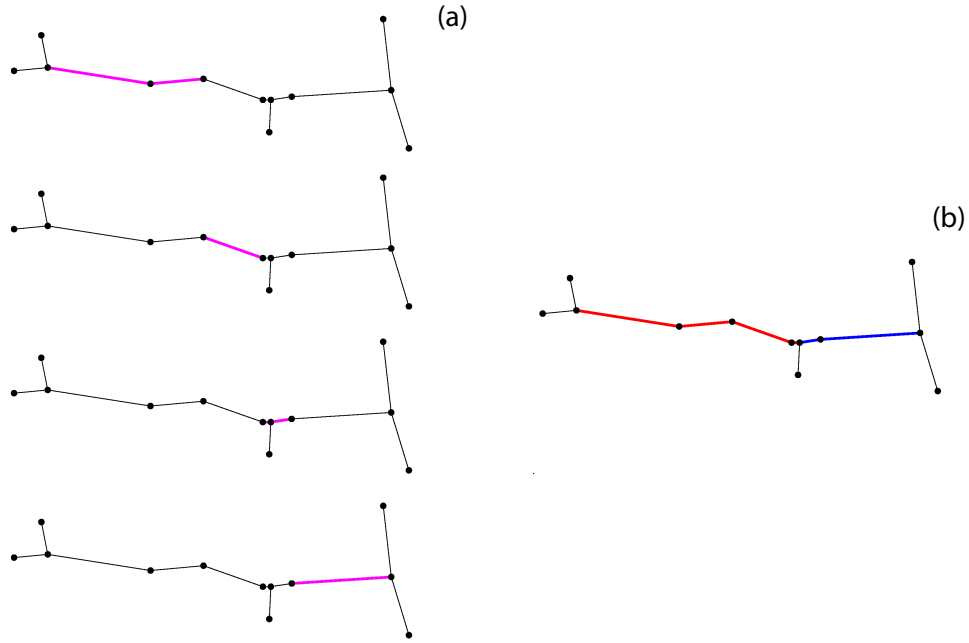


Figure 11: Resolving artificial fragmentation (a) an example of an artificially segmented fracture is shown which is saved as four polyline entries within the shapefile. These are highlighted in magenta. The first segment (top) is of topology type Y-V-V (where V used to denote a degree-2 node and Y a degree-3 node), second is a V-V segment, third is a V-Y-V segment, and the last one at the bottom is a V-Y segment. (b) The graph edge linking converts the fragmented four segments into two segments which are both of Y-Y topology type. The routine does both merge and split operations to ensure that there are no attribute table entries in the shapefile that begin or terminate in degree-2 nodes.

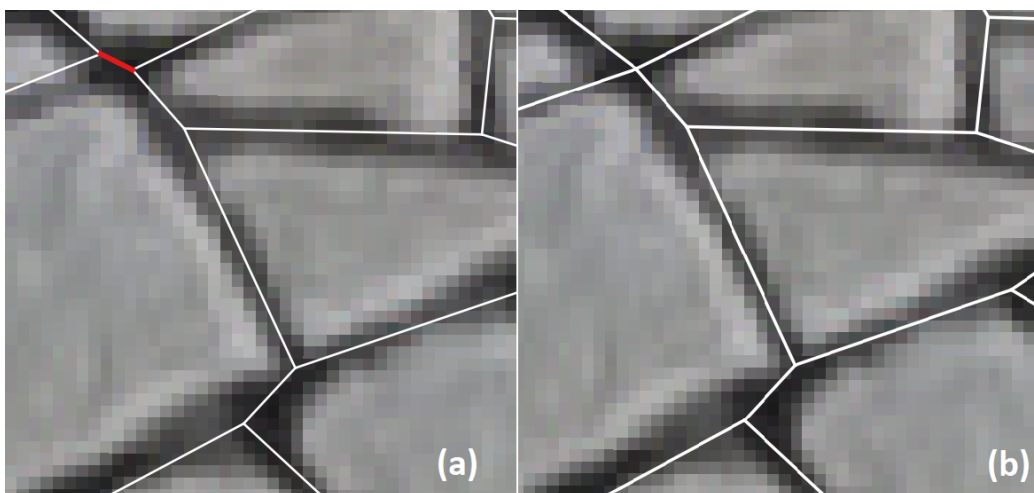


Figure 12: An example of automatically resolving a stepout by a merge operation using routine. from Area 4 (a) stepout Y-Y segment depicted in red (b) Y-Y segment removed and edges merged to form an X node

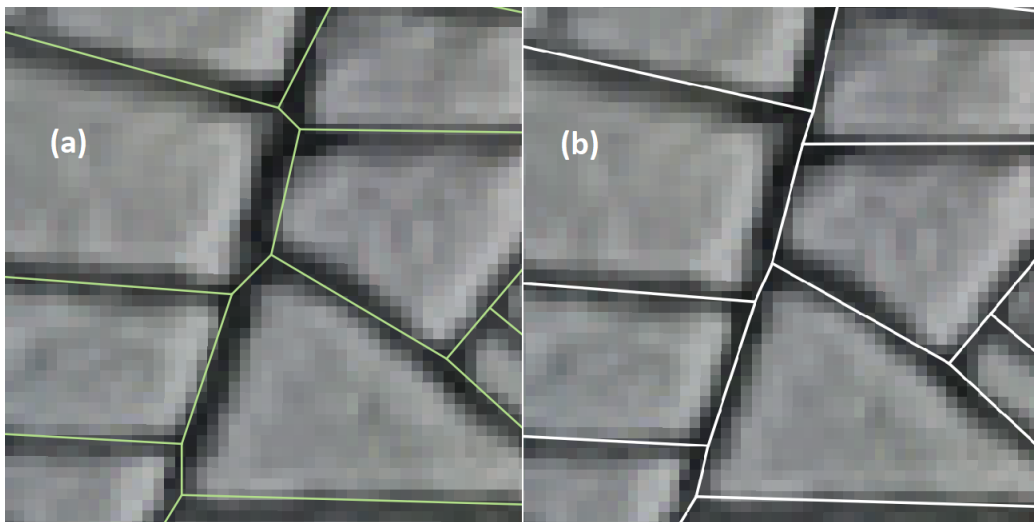


Figure 13: An example of automatically resolving a stepout by a flatten operation from Area 4 (a) stepout segments with varying strike that can cause loss in continuity when parsing for possible walks (b) stepout segments flattened

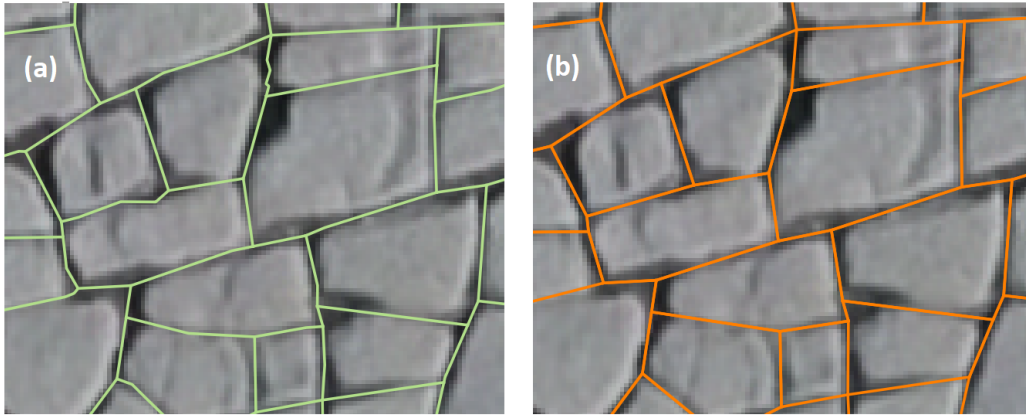


Figure 14: An example of straightening of fracture segments using from Area 5 (a) original fracture network with piece-wise linear segments and degree-2 nodes (b) fracture segments which are straightened removing the degree-2 nodes

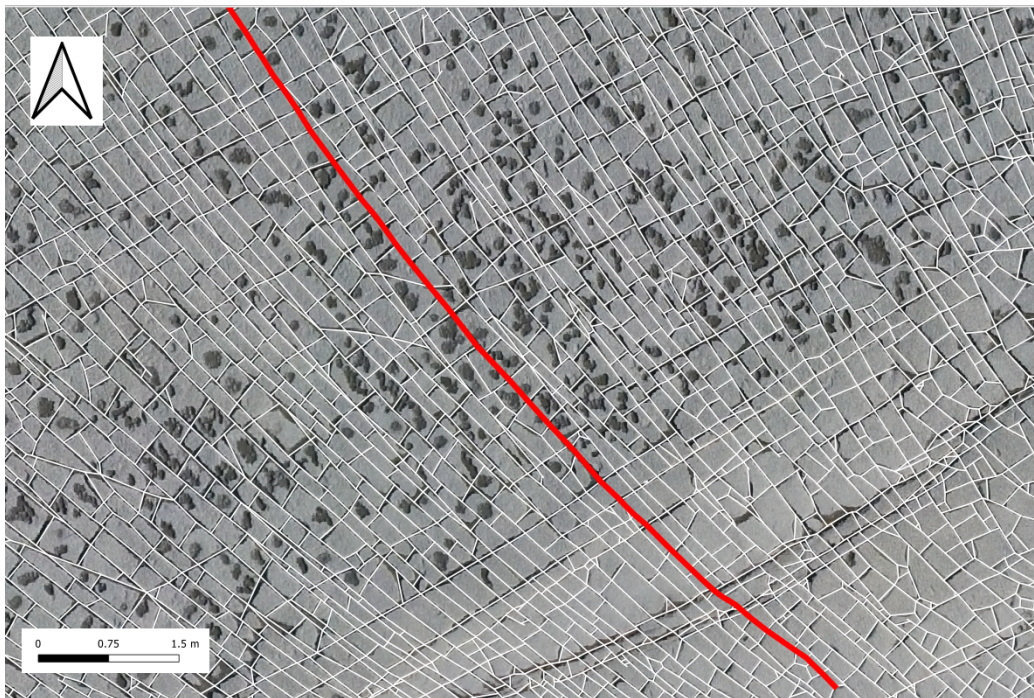


Figure 15: Continuous and sinuous fracture from Area 4 automatically joined from graph segments with a strike threshold of 20 degrees. Note that the strike of the start and end segment of the fracture vary by more than 50 degrees.

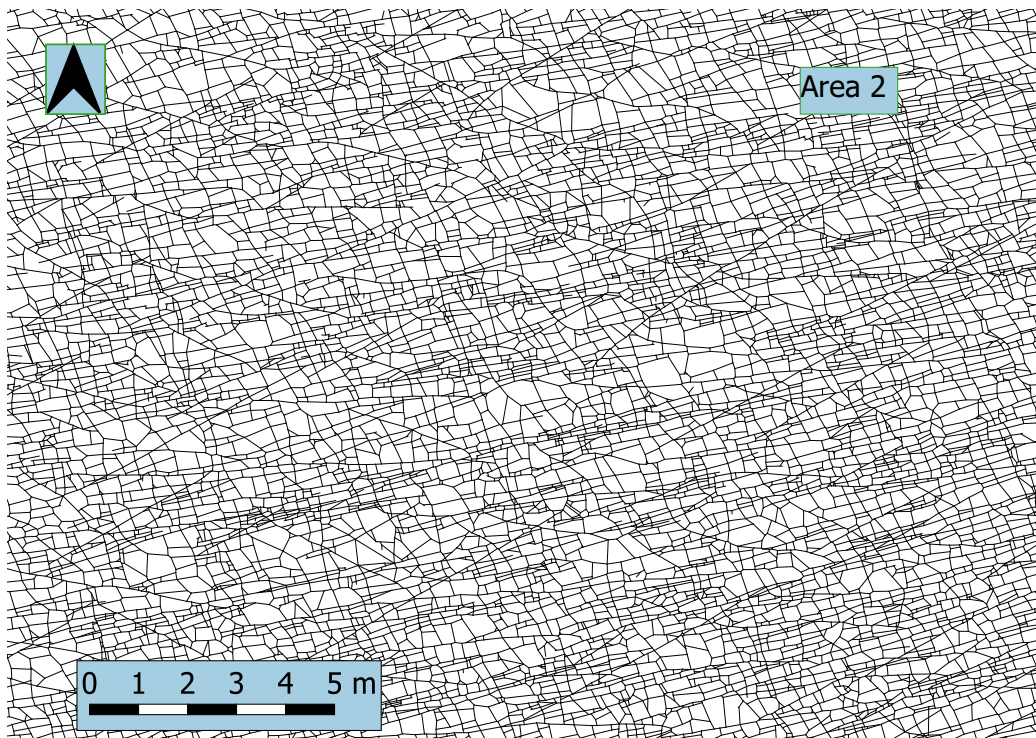


Figure 16: A zoomed in fracture network from Area 2 - Sample 1.

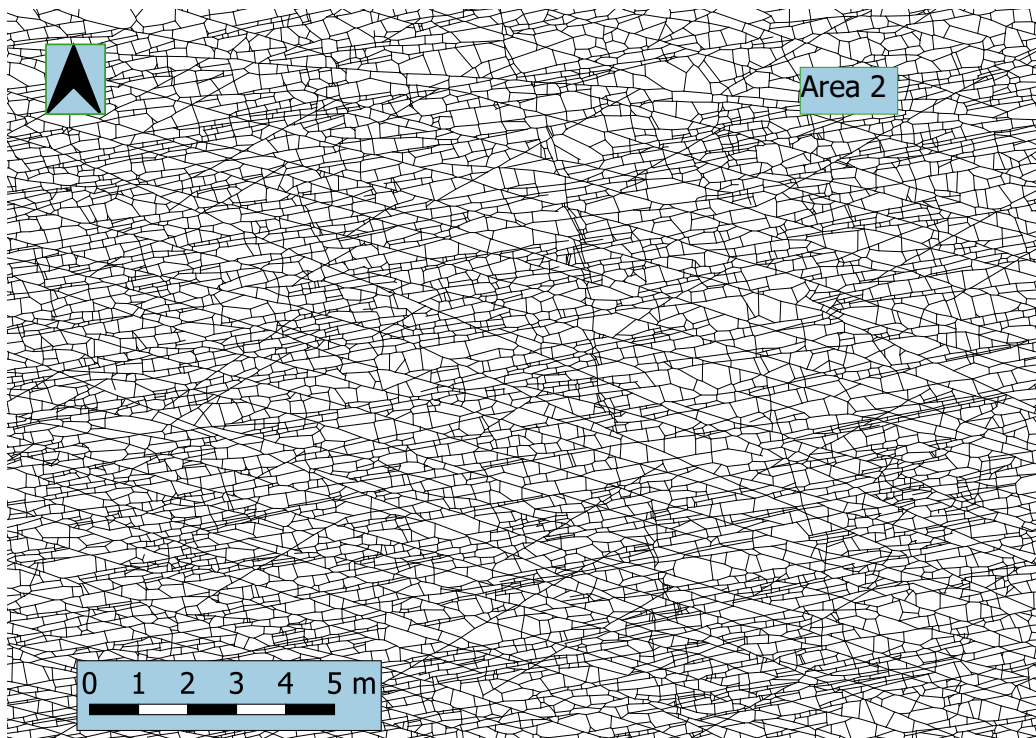


Figure 17: A zoomed in fracture network from Area 2 - Sample 2.

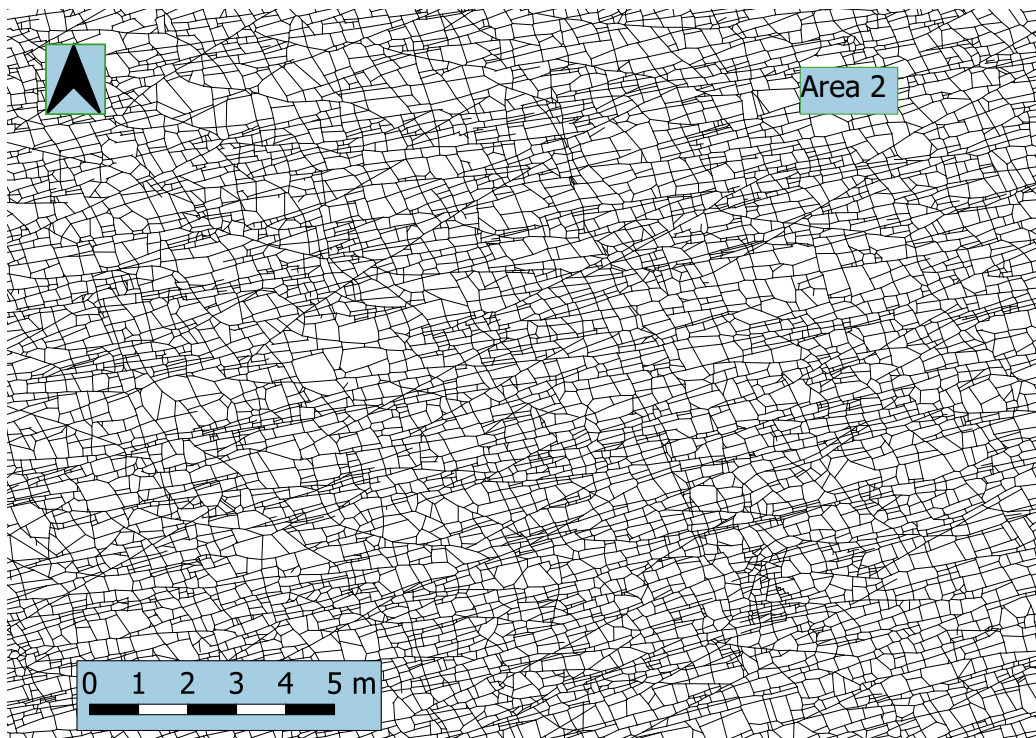


Figure 18: A zoomed in fracture network from Area 2 - Sample 3.

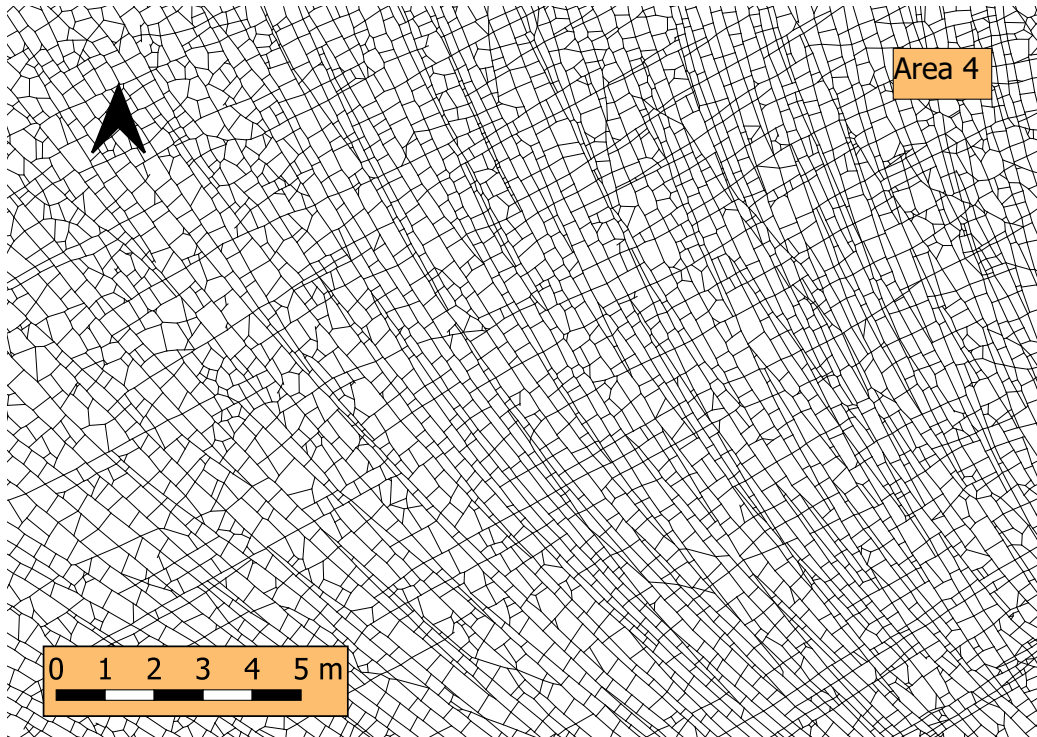


Figure 19: A zoomed in fracture network from Area 4 - Sample 1.

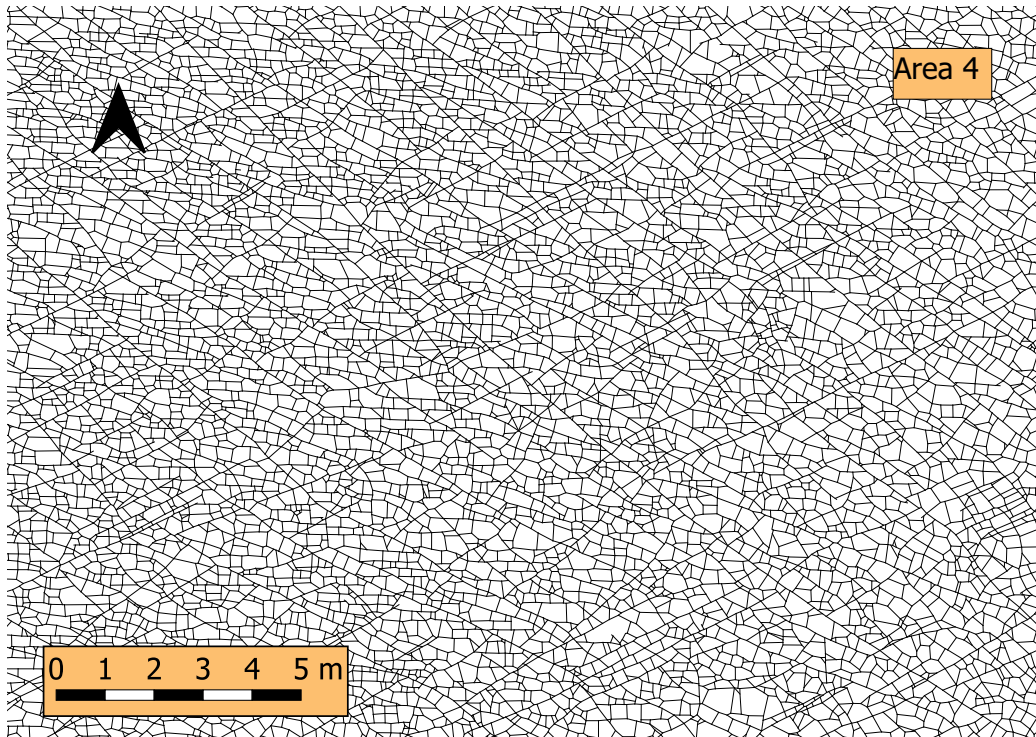


Figure 20: A zoomed in fracture network from Area 4 - Sample 2.

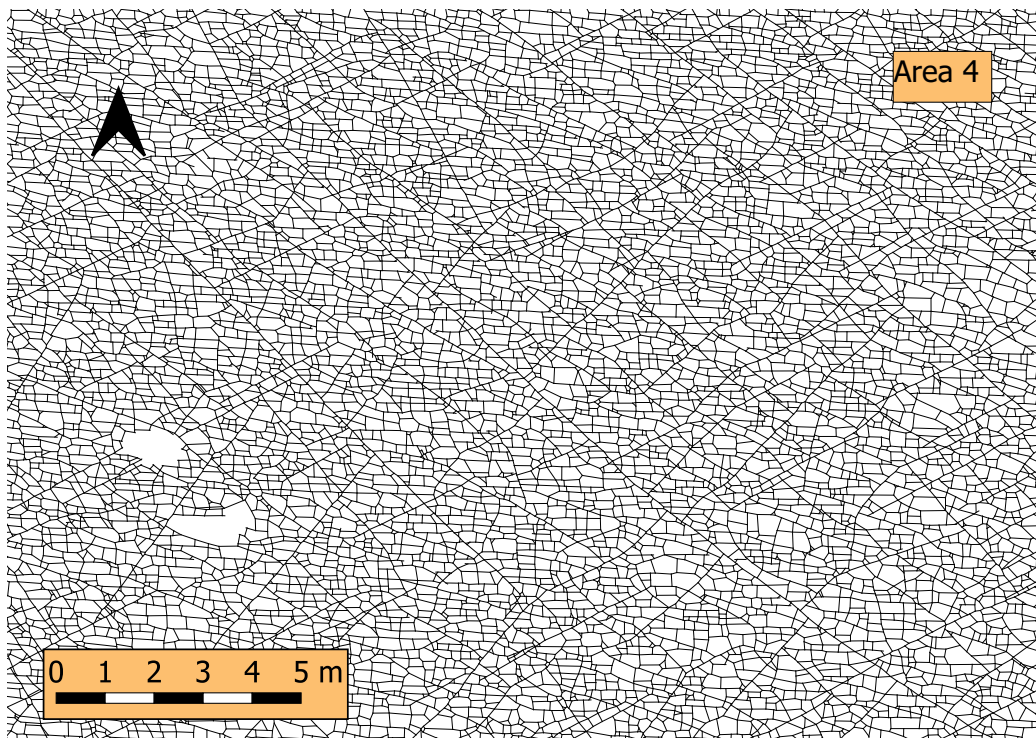


Figure 21: A zoomed in fracture network from Area 4 - Sample 3.

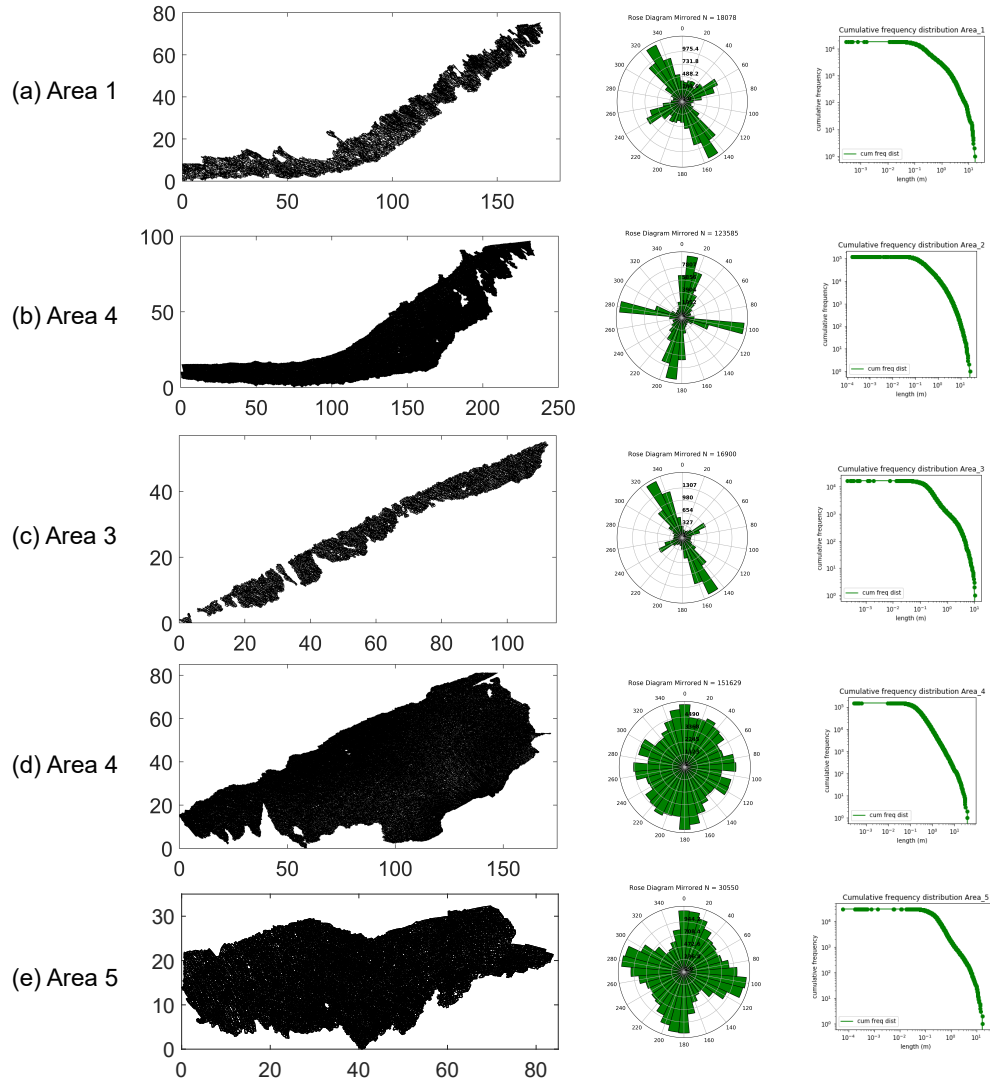


Figure 22: Fracture network trace maps for all areas with corresponding rose plots and cumulative trace length distributions (a) Area 1 (b) Area 2 (c) Area 3 (d) Area 4 (e) Area 5

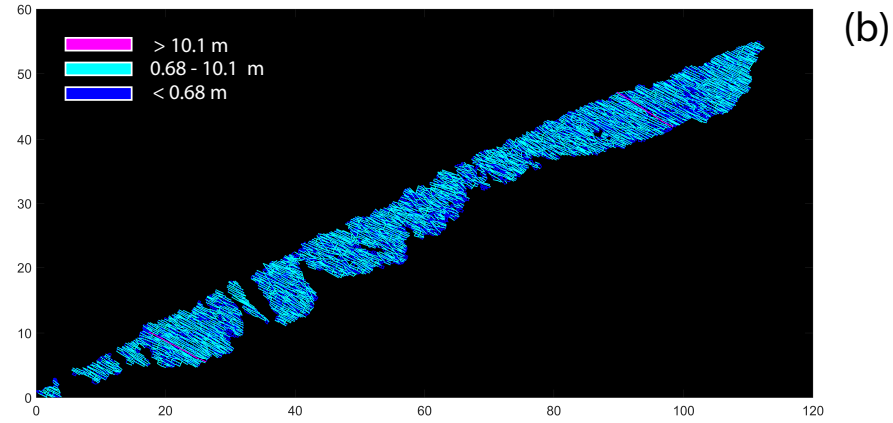
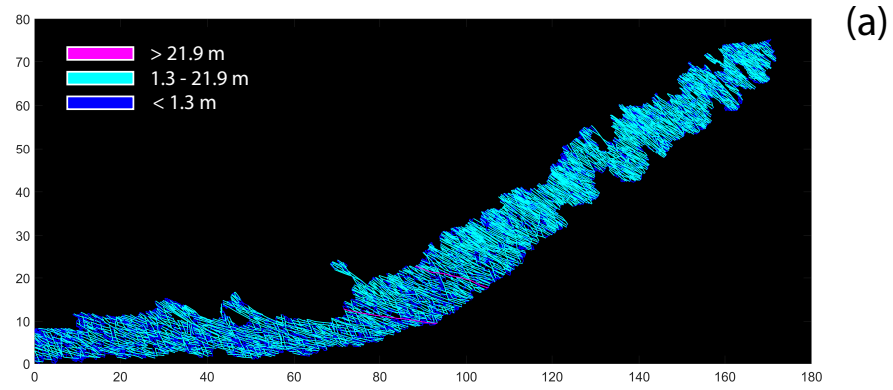


Figure 23: (a) Fractures plotted by length bins in Area 1 (b) fractures plotted by length bins in Area 3

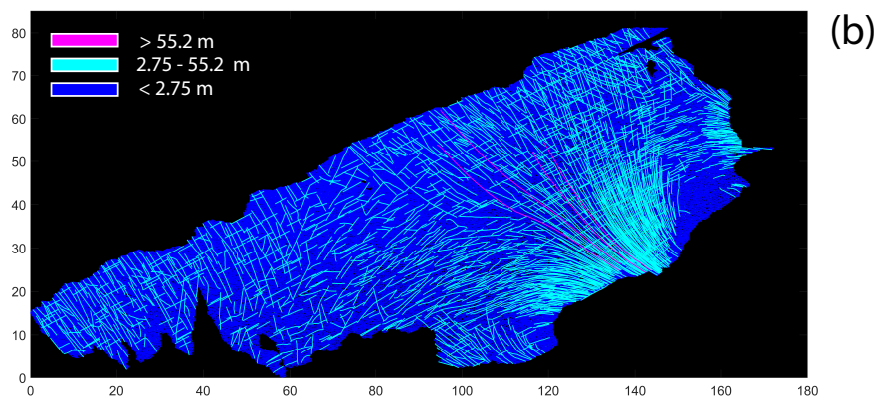
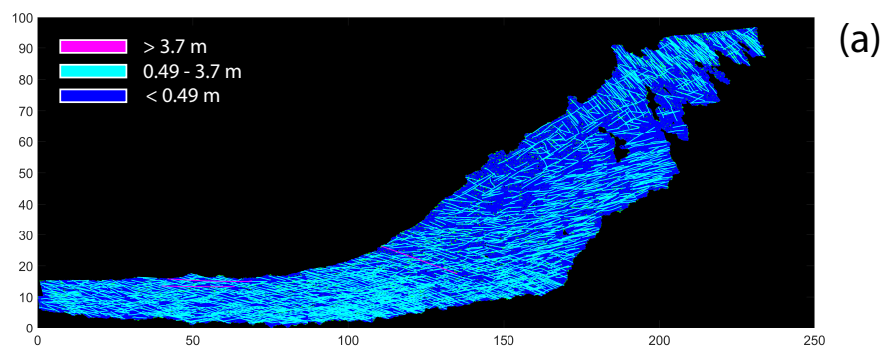


Figure 24: (a) Fractures plotted by length bins in Area 2 (b) fractures plotted by length bins in Area 4

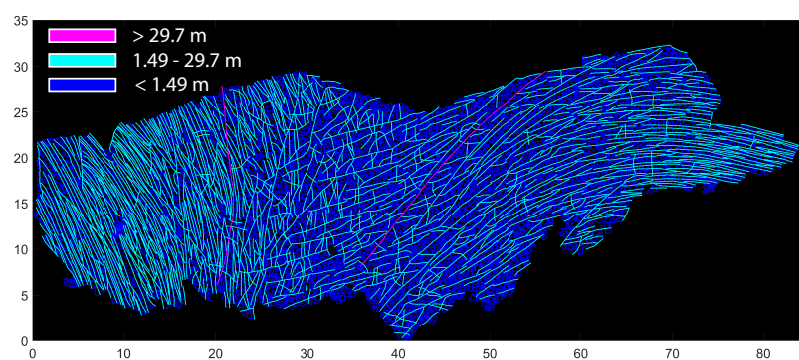


Figure 25: Fractures plotted by length bins in Area 5.

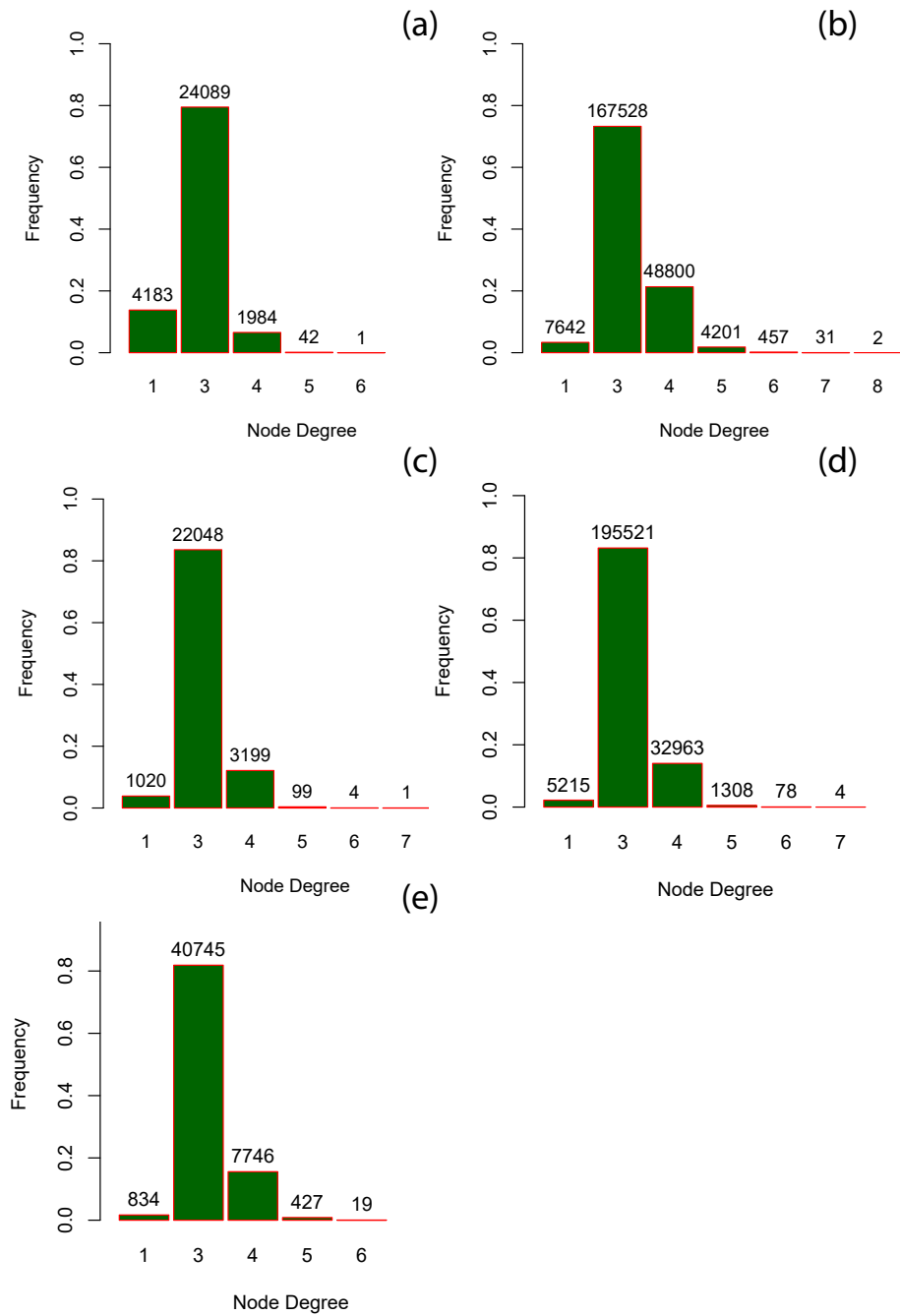


Figure 26: Degree Distributions for the primal graphs with number of nodes corresponding to each topology type (a) Area 1 (b) Area 2 (c) Area 3 (d) Area 4 (e) Area 5

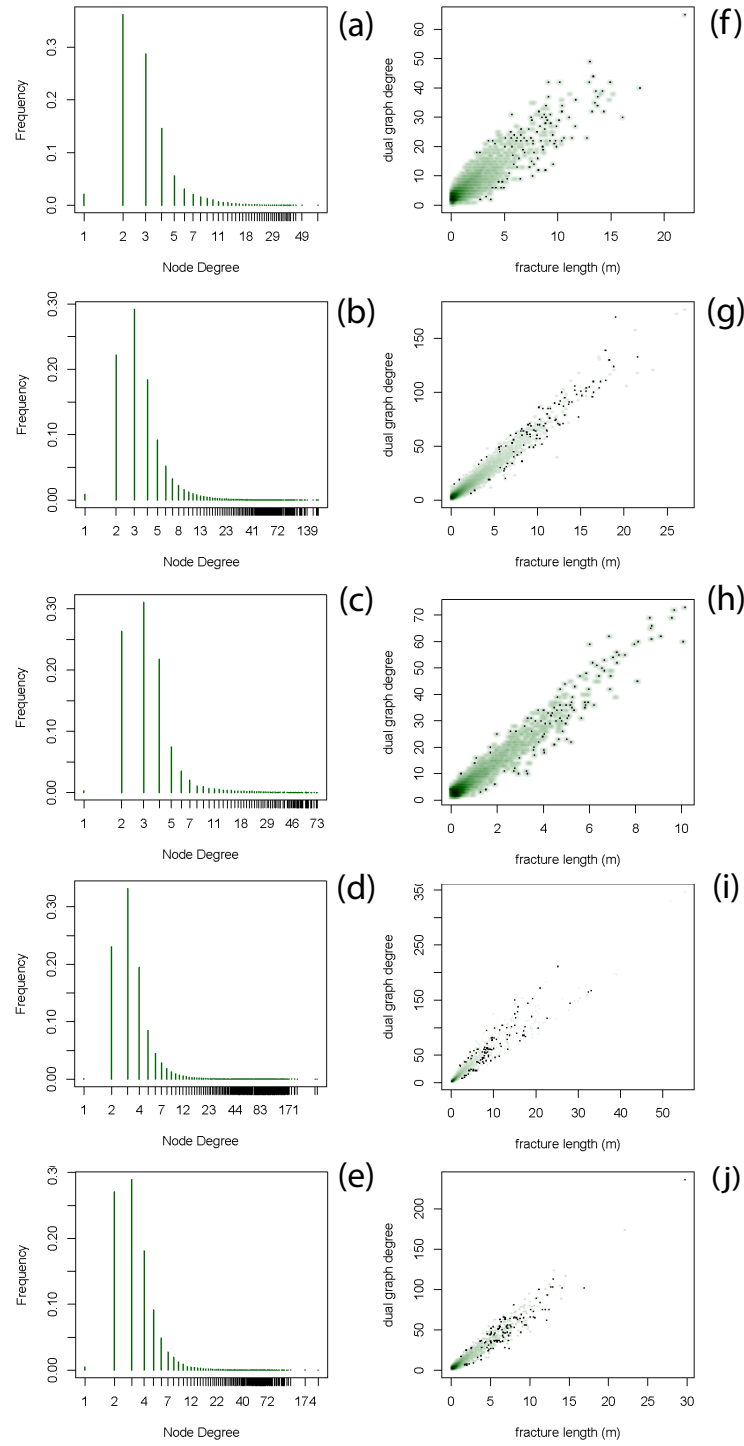


Figure 27: Degree Distributions for the dual graphs (a) Area 1 (b) Area 2 (c) Area 3 (d) Area 4 (e) Area 5 Correlation between Dual Degree and Trace Length (f) Area 1 (g) Area 2 (h) Area 3 (i) Area 4 (j) Area 5

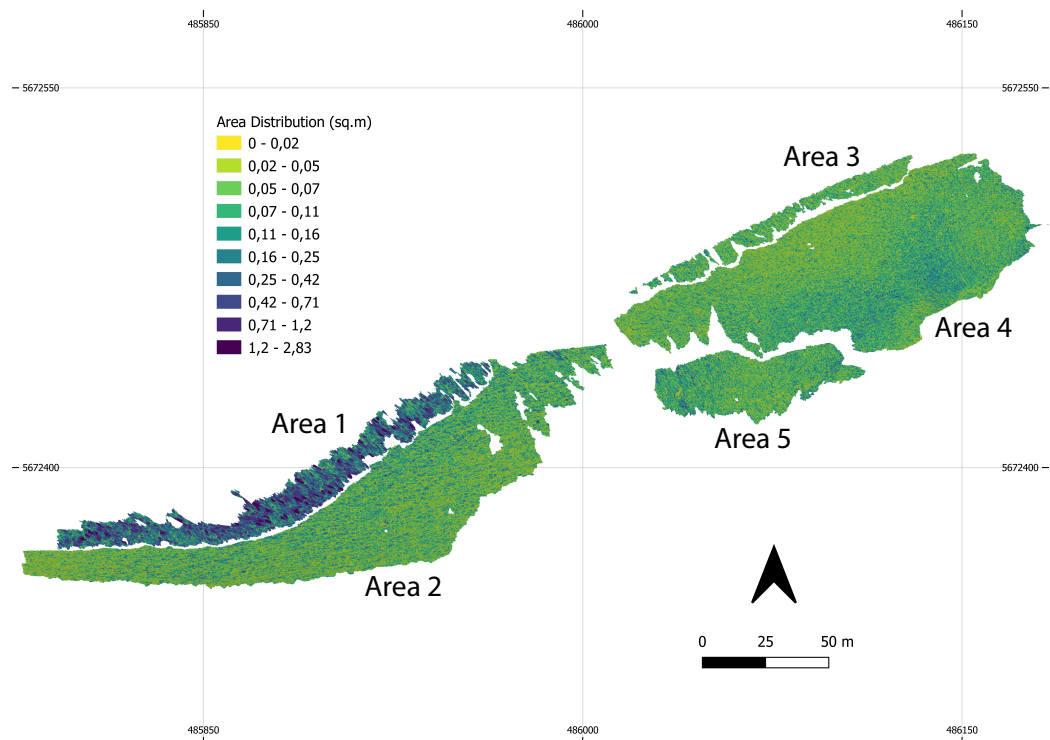


Figure 28: Spatial distribution of polygonal regions highlighting the variation in fracturing across different areas.

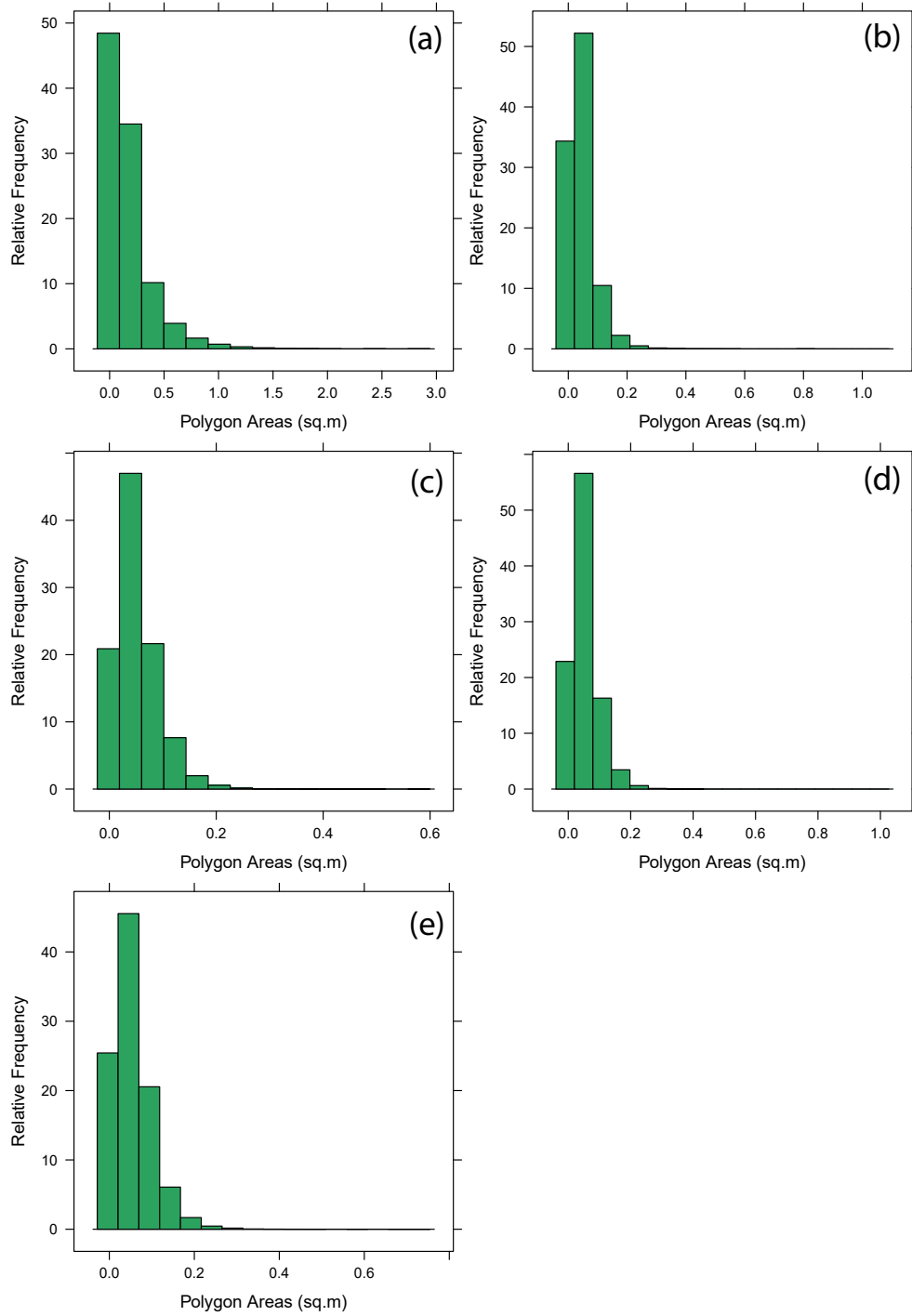


Figure 29: Bounded area distributions with relative frequency in percentages (a) Area 1 (b) Area 2 (c) Area 3 (d) Area 4 (e) Area 5

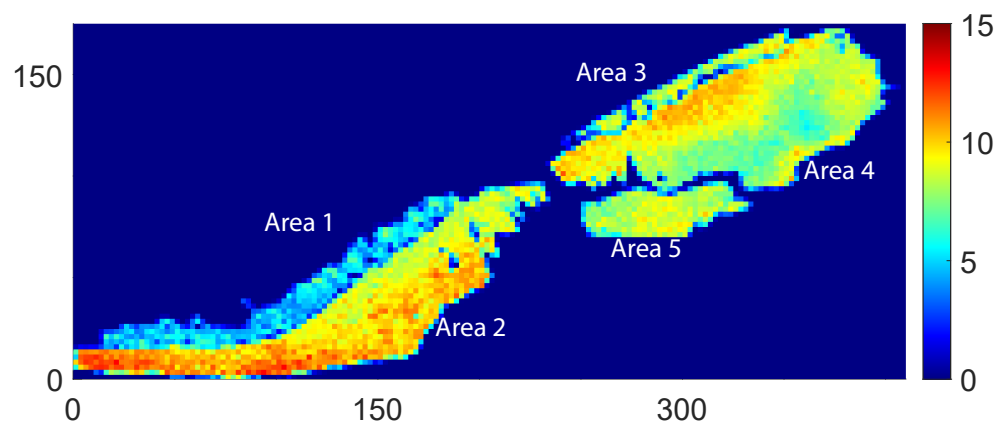


Figure 30: Fracture intensity, P_{21} (m/m^2) for all areas.

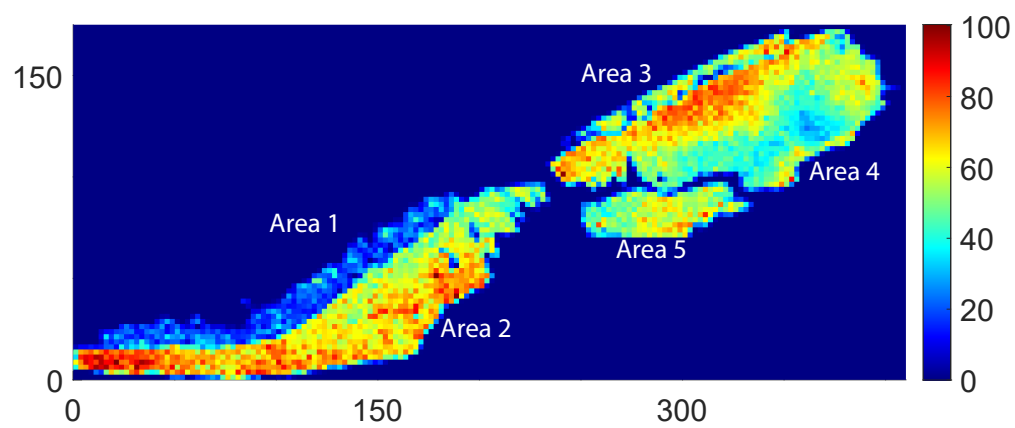


Figure 31: Fracture density, P_{20} (m^{-2}) for all areas.